

## Molecular Clouds in the Galactic Plane from $l = [59.75^\circ, 74.75^\circ]$ and $b = [-5.25^\circ, +5.25^\circ]$

2 CHUNXUE LI <sup>1,2</sup> HONGCHI WANG <sup>1,2</sup> YUEHUI MA <sup>1</sup> LIANGHAO LIN <sup>3</sup> YANG SU <sup>1</sup> CHONG LI <sup>4,5</sup> YAN SUN <sup>1</sup>  
3 XIN ZHOU <sup>1</sup> AND JI YANG <sup>1</sup>

4 <sup>1</sup>*Purple Mountain Observatory and Key Laboratory of Radio Astronomy, Chinese Academy of Sciences, 10 Yuanhua Road, Qixia*  
5 *District, Nanjing 210033, China*

6 <sup>2</sup>*School of Astronomy and Space Science, University of Science and Technology of China, 96 Jinzhai Road, Hefei 230026, China*

7 <sup>3</sup>*Max-Planck-Institut für Radioastronomie, Auf dem Hügel 69, 53121 Bonn, Germany*

8 <sup>4</sup>*School of Astronomy and Space Science, Nanjing University, 163 Xianlin Avenue, Nanjing 210023, China*

9 <sup>5</sup>*Key Laboratory of Modern Astronomy and Astrophysics (Nanjing University), Ministry of Education, Nanjing 210023, China*

### ABSTRACT

11 In this paper we present the distribution of molecular gas in the Milky Way Galactic plane from  $l =$   
12  $[59.75, 74.75]^\circ$  and  $b = [-5.25, +5.25]^\circ$ , using the MWISP  $^{12}\text{CO}/^{13}\text{CO}/\text{C}^{18}\text{O}$  emission line data. The  
13 molecular gas in this region can be mainly attributed to the Local spur, Local arm, Perseus arm, and  
14 Outer arm. Statistics of the physical properties of the molecular gas in each arm, such as excitation  
15 temperature, optical depth, and column density, are presented. Using the DBSCAN algorithm, we  
16 identified 15 extremely distant molecular clouds with kinematic distances of 14.72–17.77 kpc and  
17 masses of 363–520  $M_\odot$ , which we find could be part of the Outer Scutum-Centaurus (OSC) arm  
18 identified by Dame & Thaddeus (2011) and Sun et al. (2015). It is also possible that, 12 of these  
19 15 extremely distant molecular clouds constitute an independent structure between the Outer and  
20 the OSC arms or a spur. There exist two Gaussian components in the vertical distribution of the  
21 molecular gas in the Perseus spiral arm. These two Gaussian components correspond to two giant  
22 filaments parallel to the Galactic plane. We find an upward warping of the molecular gas in the Outer  
23 spiral arm with a displacement of around 270 pc with respect to the Galactic mid-plane.

24 *Keywords:* Interstellar medium (847); Interstellar cloud(834); Molecular clouds(1072); Surveys (1671)

### 1. INTRODUCTION

26 Star formation occurs in molecular clouds, the coldest  
27 and densest regions of the interstellar medium (ISM). It  
28 is challenging to observe  $\text{H}_2$  molecules directly via the  
29 rotational transition lines because the  $\text{H}_2$  molecules do  
30 not have permanent dipole moments. Therefore, CO,  
31 the second most abundant molecule next to  $\text{H}_2$  in the  
32 ISM, becomes the most common tracer for molecular  
33 clouds (Wilson et al. 1970). Among the three common  
34 isotopologues,  $^{12}\text{CO}$  can effectively probe the diffuse en-  
35 velopes of molecular clouds of densities of  $\sim 10^2 \text{ cm}^{-3}$ ,  
36 while  $^{13}\text{CO}$  can trace regions with intermediate den-  
37 sities of a few  $10^2$  to  $10^3 \text{ cm}^{-3}$ . In contrast,  $\text{C}^{18}\text{O}$  is  
38 a good tracer of dense molecular cores with densities  
39 as high as  $10^4 \text{ cm}^{-3}$  (e.g., Umemoto et al. 2017). So

40 far, our understanding of the physical properties and  
41 spatial distribution of molecular clouds in the Milky  
42 Way mainly comes from large-scale CO surveys, such  
43 as the early survey by Solomon et al. (1987), the CfA-  
44 Chile survey (Dame et al. 2001; Rice et al. 2016), the  
45 FCRAO Galactic Ring Survey and Outer Galaxy Sur-  
46 vey (Heyer et al. 2001; Roman-Duval et al. 2010), and  
47 the SEDIGISM (Structure, Excitation, and Dynamics of  
48 the Inner Galactic Interstellar Medium) survey (Schuller  
49 et al. 2021). These surveys helped to build a panoramic  
50 view about the Galactic molecular clouds. For exam-  
51 ple, it is found that the mass of molecular clouds ranges  
52 from  $\sim 10^1$  to  $10^6 M_\odot$ , while their sizes lie in the range  
53 from 10 to 150 pc, and their number densities are about  
54  $50\text{--}10^4 \text{ cm}^{-3}$ . Most of the molecular gas is concentrated  
55 in the so-called giant molecular clouds (GMCs) which  
56 have mass greater than  $10^4 M_\odot$ . The velocity disper-  
57 sions of clouds are about  $1 \text{ km s}^{-1}$  (Roman-Duval et al.  
58 2010). The mass function of molecular cloud is found to

59 follow a power law, with exponents within  $\sim -1.4$  to  $\sim$   
 60  $-2.2$  (Blitz 1993; Kramer et al. 1998; Rice et al. 2016).  
 61 There also exists a power law scaling relation between  
 62 the size of molecular clouds and the line width, which is  
 63 thought to originate from the turbulent motions of the  
 64 molecular gas (Larson 1981).

65 The ongoing Milky Way Imaging Scroll Painting  
 66 (MWISP) project provides us an opportunity to get a  
 67 much deeper understanding of molecular gas distribu-  
 68 tion in the Milky Way, benefiting from its wide sky cov-  
 69 erage ( $l = [12^\circ, 230^\circ]$ ), multiple spectral lines ( $^{12}\text{CO}$ ,  
 70  $^{13}\text{CO}$ , and  $\text{C}^{18}\text{O}$ ), and high-sensitivity (0.5 K per chan-  
 71 nel of  $0.17 \text{ km}^{-1}$  for  $^{12}\text{CO}$ ) (Su et al. 2019). The sky  
 72 area of Galactic longitude from  $59.75^\circ$  to  $74.75^\circ$  and  
 73 Galactic latitude from  $-5.25^\circ$  to  $5.25^\circ$  (hereafter the  
 74 “G60 region”), part of the MWISP survey, was fully ob-  
 75 served lately. This region has not been thoroughly stud-  
 76 ied before. The CfA 1.2 m telescope survey (Dame et al.  
 77 2001) has observed this region in the  $^{12}\text{CO}$  molecular  
 78 line, but its spatial resolution is quite low. The Exeter-  
 79 FCRAO (EXFC) survey (Roman-Duval et al. 2016) ob-  
 80 served two regions,  $l = [55, 100]^\circ$ ,  $b = [-1.4, 1.9]^\circ$ , and  
 81  $l = [135, 195]^\circ$ ,  $b = [-3.6, 3.6]^\circ$ . The distribution in  
 82 the face-on view of the Milky Way of molecular gas in  
 83 the first region was presented in Figure 9 of Roman-  
 84 Duval et al. (2016). This region contains active past  
 85 and ongoing star formation, as shown by the presence  
 86 of supernova remnants (SNRs) (Green 2019) and H II  
 87 regions/candidates (Anderson et al. 2014). We focus in  
 88 this work on the molecular gas distribution and phys-  
 89 ical properties using the  $^{12}\text{CO}$ ,  $^{13}\text{CO}$ , and the  $\text{C}^{18}\text{O}$   $J$   
 90  $= 1-0$  line data from the MWISP project. The high-  
 91 sensitivity of the MWISP data also provides an opportu-  
 92 nity to identify extremely distant molecular clouds (e.g.,  
 93 Sun et al. 2015). Dame & Thaddeus (2011) found a seg-  
 94 ment of the Outer Scutum-Centaurus arm at a Galacto-  
 95 centric distance of about 15 kpc using the data from the  
 96 CfA 1.2 m telescope survey. We will search for distant  
 97 molecular clouds corresponding to the OSC arm in the  
 98 part of the sky investigated in this work.

99 The paper is organized as follows. The observations  
 100 are presented in Section 2, and the results are given in  
 101 Section 3. The discussion about the vertical distribution  
 102 of molecular gas in the direction vertical to the Galactic  
 103 plane is presented in Section 4, and we give our summary  
 104 in Section 5.

## 105 2. OBSERVATIONS

### 106 2.1. CO data

107 The observation of the G60 region is part of the  
 108 MWISP survey and was taken from 2016 to 2020, using  
 109 the 13.7 m millimeter-wavelength telescope of the Pur-

110 ple Mountain Observatory (PMO-13.7m) at Delingha,  
 111 China. The telescope is equipped with the Supercon-  
 112 ducting Spectroscopic Array Receiver (SSAR), with  $3 \times 3$   
 113 beams. The  $^{12}\text{CO}$ ,  $^{13}\text{CO}$ , and  $\text{C}^{18}\text{O}$  ( $J = 1-0$ ) line emis-  
 114 sion were observed simultaneously with the  $^{12}\text{CO}$  ( $J =$   
 115  $1-0$ ) emission being contained in the upper sideband,  
 116 while the  $^{13}\text{CO}$  ( $J = 1-0$ ) and  $\text{C}^{18}\text{O}$  ( $J = 1-0$ ) emission  
 117 in the lower sideband. The back end for each sideband  
 118 is a fast Fourier transform spectrometer (FFTS) which  
 119 has a total bandwidth of 1 GHz and 16,384 frequency  
 120 channels, providing a spectral resolution of 61 kHz, cor-  
 121 responding to velocity resolution of  $0.158 \text{ km s}^{-1}$  at 115  
 122 GHz and  $0.167 \text{ km s}^{-1}$  at 110 GHz, respectively (Shan  
 123 et al. 2012).

124 The observations cover the sky region of Galactic lon-  
 125 gitude of  $l = [59.75, 74.75]^\circ$  and Galactic latitude of  $b =$   
 126  $[-5.25, 5.25]^\circ$ , and were made in the position-switch on-  
 127 the-fly (OTF) mode with a typical scan rate and dump  
 128 time of 50 (or 75)  $''/\text{s}$  and 0.3 (or 0.2) s, respectively.  
 129 The surveyed region is divided into individual cells of  $30'$   
 130  $\times 30'$ . Each cell was scanned at least twice, along the  
 131 directions of Galactic longitude and Galactic latitude,  
 132 to reduce scanning effects. The pointing accuracy of the  
 133 telescope is about  $5''$  in all observational epochs, and  
 134 the half-power beam widths are about  $55''$  and  $52''$  at  
 135 110 GHz and 115 GHz, respectively. The antenna tem-  
 136 perature ( $T_A^*$ ) is corrected to the main beam brightness  
 137 temperature ( $T_{\text{mb}}$ ) using  $T_{\text{mb}} = T_A^* / \eta_{\text{mb}}$  during the  
 138 observation, where the value of the main beam efficiency  
 139 ( $\eta_{\text{mb}}$ ) can be obtained from the annual status report<sup>1</sup> of  
 140 the telescope. All the raw data were reduced using the  
 141 GILDAS-CLASS<sup>2</sup> package. The final data were regrid-  
 142 ded into  $30'' \times 30''$  pixels in the directions of Galactic  
 143 longitude and Galactic latitude and converted to FITS  
 144 files. The median RMS noise level of the molecular line  
 145 is  $\sim 0.5$  K per channel at the  $^{12}\text{CO}$  wavelength and  $\sim 0.3$   
 146 K per channel at the  $^{13}\text{CO}$  and  $\text{C}^{18}\text{O}$  wavelengths. For  
 147 more details about the MWISP project, please refer to  
 148 Su et al. (2019).

## 149 3. RESULTS

### 150 3.1. Average Spectra

151 Figure 1 shows the average spectra of the  $^{12}\text{CO}$ ,  $^{13}\text{CO}$ ,  
 152 and  $\text{C}^{18}\text{O}$   $J = 1-0$  line emission in the whole G60 re-  
 153 gion. The  $^{12}\text{CO}$  spectrum shows strong emission within  
 154 the velocity range from  $\sim -30$  to  $40 \text{ km s}^{-1}$ , while the  
 155  $^{13}\text{CO}$  emission is mainly contained within a narrower  
 156 velocity range, i.e.,  $[-25, 25] \text{ km s}^{-1}$ . The average spec-

<sup>1</sup> <http://english.dlh.pmo.cas.cn/fs/>

<sup>2</sup> <http://www.iram.fr/IRAMFR/GILDAS/>

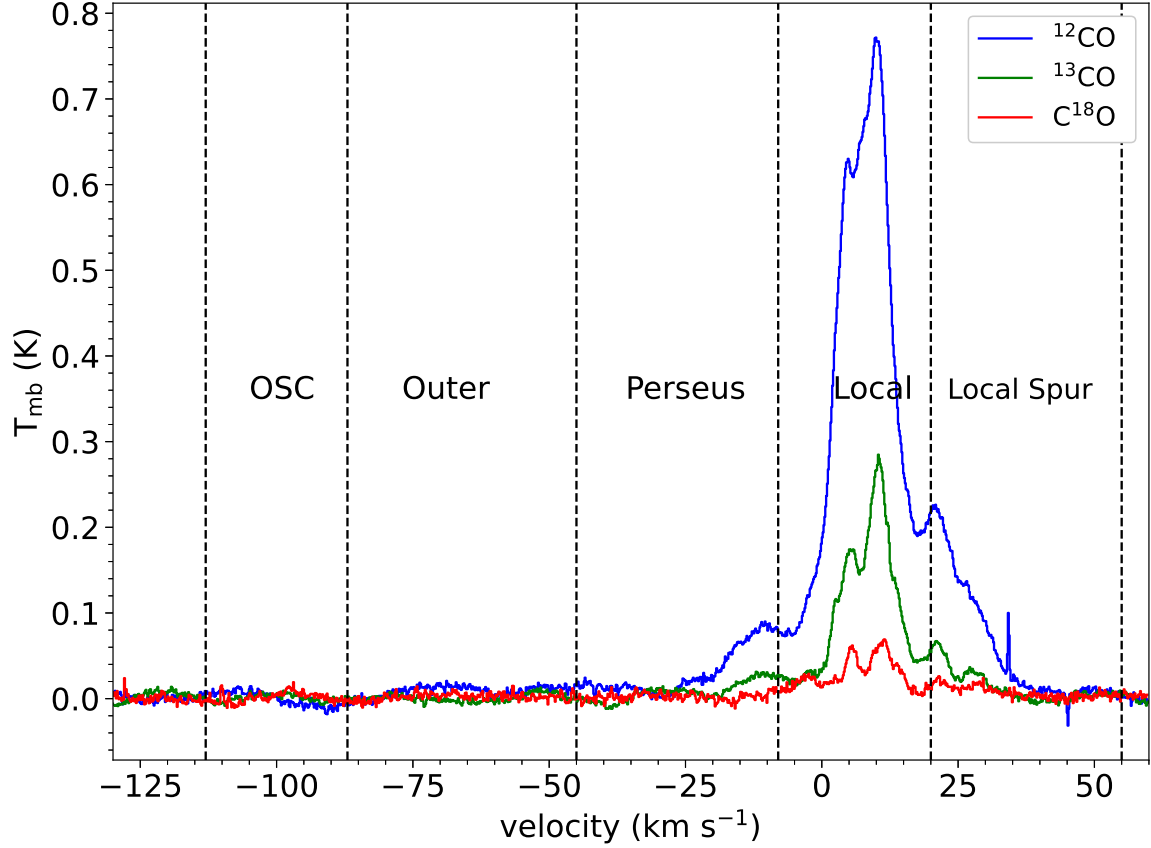
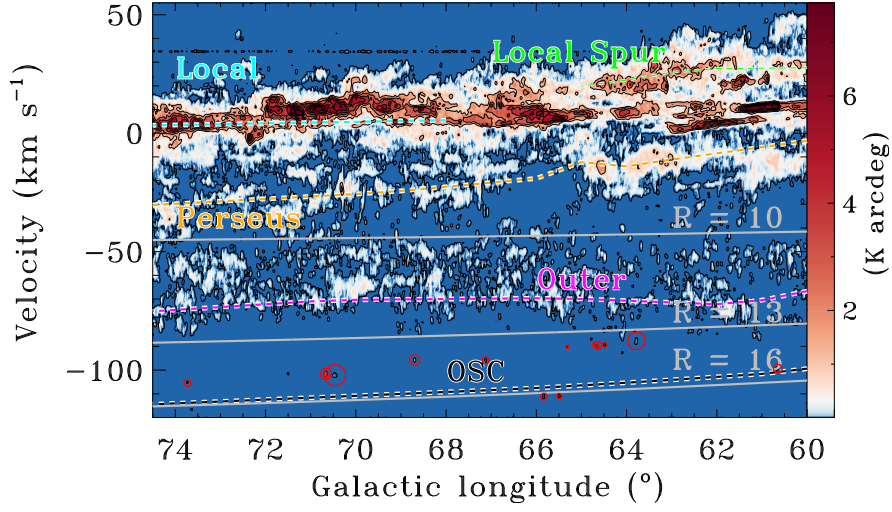
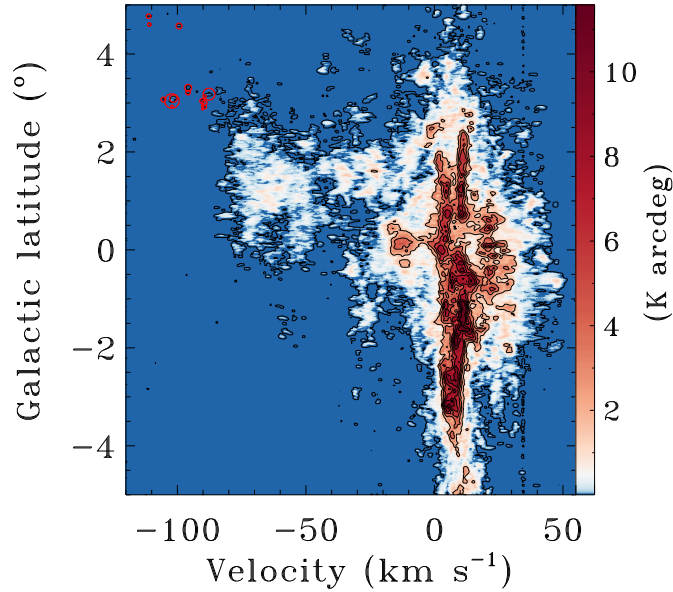


**Figure 1.** Average spectra of the G60 region, with blue, green, and red showing the  $^{12}\text{CO}$ ,  $^{13}\text{CO}$ , and  $\text{C}^{18}\text{O}$   $J = 1-0$  line emission, respectively. The  $^{12}\text{CO}$  spectrum contains spikes at  $35 \text{ km s}^{-1}$  and  $45 \text{ km s}^{-1}$ , the  $^{13}\text{CO}$  spectrum at  $-74 \text{ km s}^{-1}$ , and the  $\text{C}^{18}\text{O}$  spectrum at  $-127$  and  $-109 \text{ km s}^{-1}$ . These spikes are caused by bad channels. According to Reid et al. (2019), spiral arms, from near to far, in the portion of the Galactic plane investigated in this work, are the Local arm, Local Spur, Perseus arm, Outer arm, and OSC arm. The velocity ranges of these arms are marked with vertical dashed lines. The  $^{12}\text{CO}$ ,  $^{13}\text{CO}$ , and  $\text{C}^{18}\text{O}$  spectrum are averaged on the positions that show  $^{12}\text{CO}$ ,  $^{13}\text{CO}$ , and  $\text{C}^{18}\text{O}$  emission brightness above two times their RMS noise level in at least five, four, and three contiguous channels, respectively.

157 trum of  $\text{C}^{18}\text{O}$  shows emission between  $-25$  and  $40$  km  
158  $\text{s}^{-1}$ . The spikes at  $35$   $\text{km s}^{-1}$  and  $45$   $\text{km s}^{-1}$  in the  
159  $^{12}\text{CO}$  spectrum,  $-74$   $\text{km s}^{-1}$  in  $^{13}\text{CO}$ ,  $-127$  and  $-109$   
160  $\text{km s}^{-1}$  in  $\text{C}^{18}\text{O}$  are all due to bad channels. Only spec-  
161 tra with peak intensities above  $3\sigma_{RMS}$  and containing  
162 adequate number of contiguous channels that have in-  
163 tensities above  $2\sigma_{RMS}$  are considered as the spectra of  
164 detection. For  $^{12}\text{CO}$ ,  $^{13}\text{CO}$ , and  $\text{C}^{18}\text{O}$ , this number of  
165 contiguous channels is five, four, and three, respectively.



(a)



(b)

**Figure 2.** (a) Longitude-velocity diagram of the  $^{12}\text{CO}$  emission, integrated within  $b = -5^\circ$  to  $5^\circ$ . The colored dashed lines represent the  $l$ - $v$  position of the Local Spur, Local, Perseus, Outer, and Outer-Scutum-Centaurus (OSC) arms from Reid et al. (2019). Constant Galactocentric distances of 10, 13, and 16 kpc are indicated with grey lines. These lines are calculated with the rotation curve of Reid et al. (2019). (b) Latitude-velocity diagram of the  $^{12}\text{CO}$  emission, integrated within  $l = 60^\circ$  to  $74.5^\circ$ . The red circles mark molecular clouds located in the OSC arm (for details, see Section 3.6).

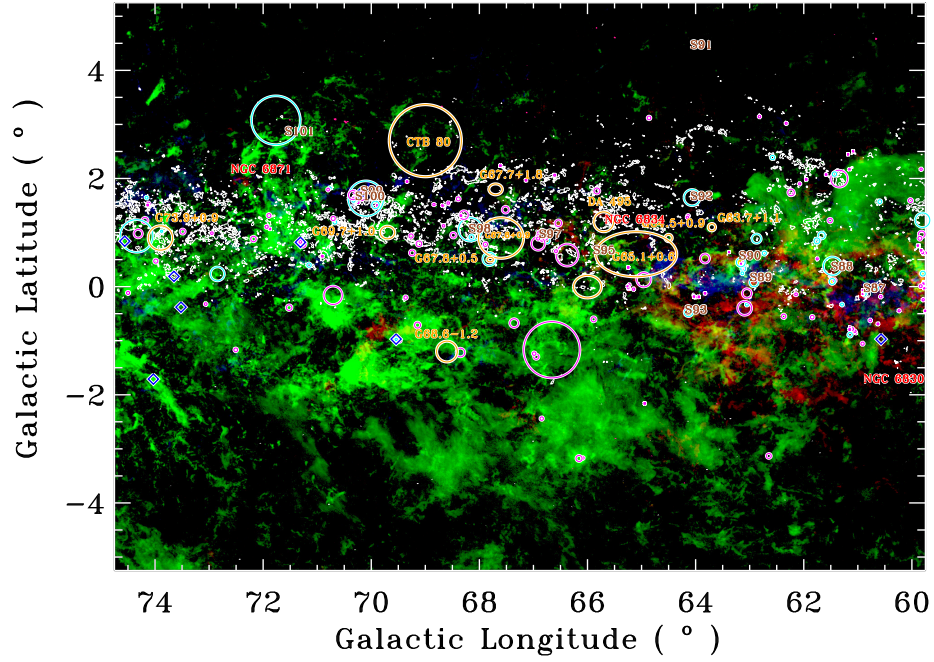


**Figure 3.** Color-coded intensity maps of  $^{12}\text{CO}$  emission in different velocity ranges. The integrated intensity of  $^{12}\text{CO}$  emission in velocity ranges from 20 to 55,  $-8$  to 20, and  $-45$  to  $-8$   $\text{km s}^{-1}$  are shown by red, green, and blue colors, respectively. White contours represent intensity integrated in  $[-87, -45]$   $\text{km s}^{-1}$ . The orange ellipses show the locations of known SNRs (Green 2019) in this region. The magenta circles and the cyan circles show the locations of the H II region and H II candidates from the WISE catalog (Anderson et al. 2014). The names of the H II regions in the Sharpless catalog (Sharpless 1959) are represented by brown letters, and the names of the SNRs are denoted by orange. The masers (Reid et al. 2019) are indicated by blue diamonds. Three active star-forming regions, NGC 6830, NGC 6834, and NGC 6871 are shown in red letters.

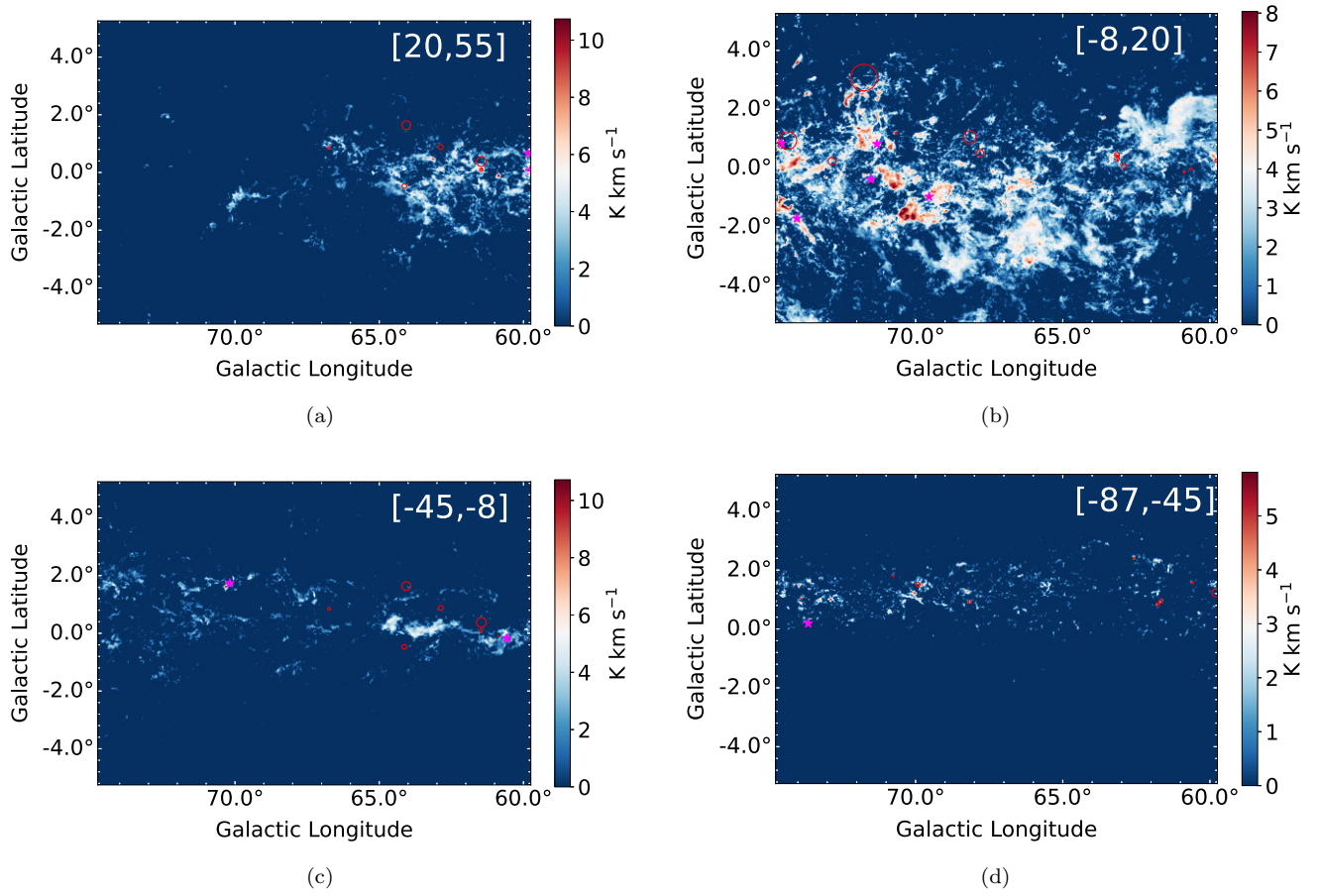


**Figure 4.** Integrated intensity maps of  $^{12}\text{CO}$  emission in the (a) Local Spur, (b) Local arm, (c) Perseus arm, and (d) Outer arm. The magenta pentagrams mark the positions of the associated masers from Reid et al. (2019). The velocity range of each arm is given in the top right corner of each panel. The red circles indicate the locations of H II region and candidates in the corresponding velocity range.

### 3.2. Position-Velocity Distribution and Velocity Ranges of Spiral Arms

The l-v and b-v diagrams of the  $^{12}\text{CO}$  line emission are shown in Figure 2. The integrated range of the l-v diagram is between  $b = -5^\circ$  and  $b = 5^\circ$ , while that for the b-v diagram is between  $l = 60^\circ$  and  $l = 74.5^\circ$ . In the two diagrams, the noise has been clipped using the criteria mentioned in Section 3.1. The  $34 \text{ km s}^{-1}$  bad channels show as thin horizontal and vertical lines in the l-v and b-v diagrams, respectively. The traces of the Galactic spiral arms, adopted from Reid et al. (2019), are marked as dashed lines in the l-v map. Based on the rotation curve from Reid et al. (2019), we calculated Galactocentric distances ( $R$ ). The lines for  $R = 10, 13, \text{ and } 16 \text{ kpc}$  are shown in the l-v diagram. The molecular clouds located in the OSC arm are indicated by red circles (for details, see Section 3.6). According to the l-v distribution and also the average spectra in Figure 1, the molecular emission contained in velocity intervals of  $[20, 55]$ ,  $[-8, 20]$ ,  $[-45, -8]$ ,  $[-87, -45]$ ,  $[-119, -87] \text{ km s}^{-1}$  is attributed to molecular gas located in the Local Spur, Local, Perseus, Outer, and OSC spiral arms, respectively. From Figure 2 (a), we can see that the molecular gas in this section of the Galactic disk well follows the spiral arms or the Local spur. Both the molecular gas and the spiral arms run nearly horizontal, i.e., along the direction of Galactic longitude, with the Local spur, the Perseus arm, and the OSC arm being diagonally oriented slightly. Ideally, we should cut the l-v diagram into diagonal strips to attribute the molecular gas to each arm or the Local spur. However, it is hard to exactly define the boundary between the Local spur and the Local arm, and the one between the Local arm and the Perseus arm. For simplicity, we just used the horizontal cuts as given above. From Figure 2 (a), we can see that this provides a clean enough separation for most of the molecular gas, although there are some ambiguity between the Local spur and the Local arm, and between the Local arm and the Perseus arm. Significant  $^{12}\text{CO}$  emission is concentrated in the Local Spur, Local arm, and the Perseus arm. Molecular clouds in the Outer arm exhibit fragmented distribution. As shown in the b-v diagram (Figure 2 b), the molecular emission in the Outer spiral arm is mainly distributed above  $b = 0^\circ$ , which may be the result of warping in the gas disk of our Galaxy (Westerhout 1957; Wouterloot et al. 1990). The l-v and b-v diagrams of the  $^{13}\text{CO}$  emission in the G60 region are presented in Figure 12 in the Appendix.

### 3.3. Spatial Distribution

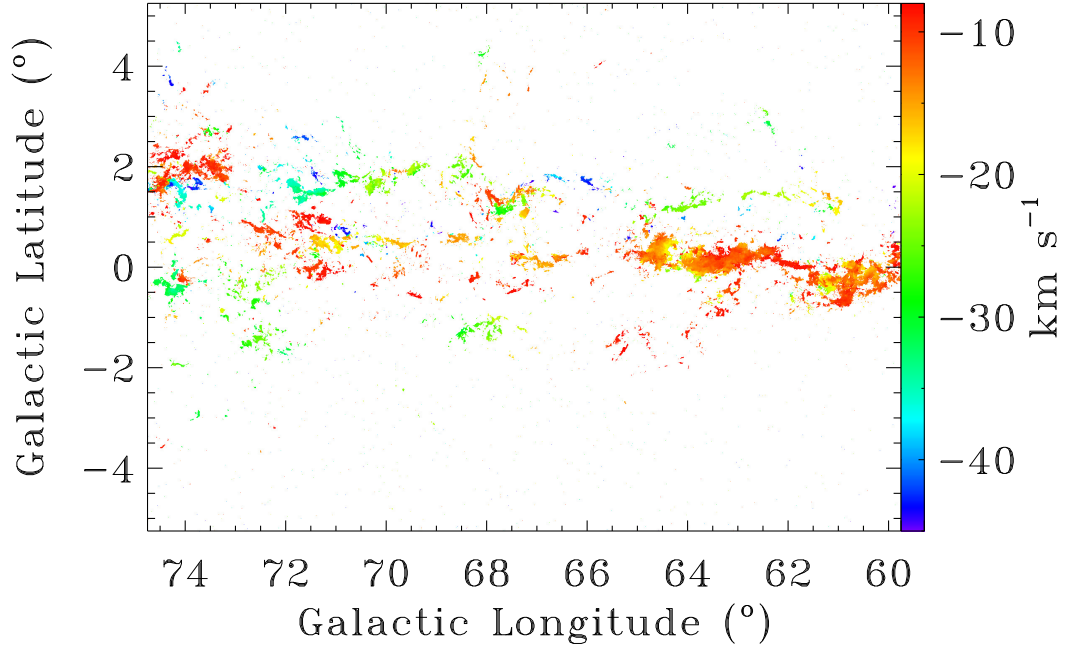
The sky distribution of the molecular gas in the G60 region is presented in Figure 3. Red, green, and blue

colors correspond to the  $^{12}\text{CO}$  intensities integrated in the velocity range of the Local Spur, Local arm, and Perseus arm, respectively, and the white contours represent the integrated intensity of molecular gas in the Outer arm. The masers (Reid et al. 2019) are marked with blue diamonds. The known SNRs (Green 2019) are indicated with orange ellipses. The H II regions and the H II region candidates from Anderson et al. (2014) are shown with magenta circles and cyan circles, respectively. The three prominent star-forming regions in the G60 region, NGC 6830, NGC 6834, and NGC 6871 are shown with red letters. The names of the SNRs are denoted with orange letters, and the names of H II regions from the Sharpless catalog (Sharpless 1959) with brown letters. In this figure, the most conspicuous component is the Local arm (green). The molecular gas in the Local Spur is mainly distributed in regions of  $l \leq 67^\circ$  and exhibits more clumpiness than gas in the Local arm. The H II regions and candidates are more spatially coincident with the molecular gas in the Local Spur and the Perseus/Outer arm regions than with the molecular gas in the Local arm.

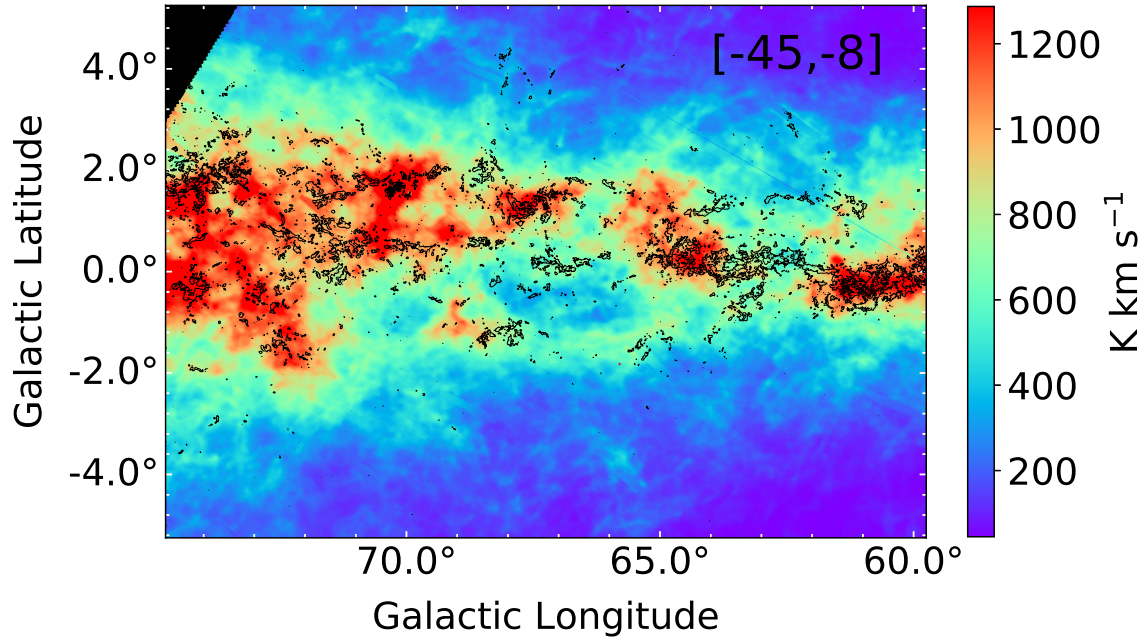
For a closer inspection, we individually present the integrated  $^{12}\text{CO}$  emission intensity maps of the Local Spur, Local arm, Perseus arm, and Outer arm in Figure 4. The differences of molecular gas in the distribution and morphology between the Local spur and Local arm are obvious. The most prominent feature of the molecular gas in the Perseus arm is that it can be divided into two nearly parallel layers along the Galactic longitude direction, i.e., a layer at  $b = 0^\circ$  and another layer at around  $b = 2^\circ$ . For the Outer arm, molecular gas is all located above  $b = 0^\circ$  and it is concentrated in small compact cores. The masers (Reid et al. 2019) associated with the molecular gas in each arm are indicated with magenta pentagrams in Figure 4. The integrated intensity map of the  $^{13}\text{CO}$  emission for each arm is presented in Figure 13 in Appendix. The velocity channel maps of the region for the  $^{12}\text{CO}$  emission are presented in Figures 14–17 in the Appendix. As the  $^{13}\text{CO}$  emission is much weaker compared with the  $^{12}\text{CO}$  emission, we do not present the  $^{13}\text{CO}$  velocity channel maps.

Figure 5 presents the intensity-weighted centroid velocity map of the  $^{12}\text{CO}$  emission from the Perseus arm. As shown in Figure 5, the two layers of molecular gas in the Perseus arm located at around  $b = 0^\circ$  and  $b = 2^\circ$  also exhibit velocity coherence. The layer at  $b = 2^\circ$  possesses velocities from  $-30$  to  $-20 \text{ km s}^{-1}$ , while the layer at  $b = 0^\circ$  has velocities from  $-20$  and  $-10 \text{ km s}^{-1}$ . These two layers show a systematic velocity difference of about  $10 \text{ km s}^{-1}$ , with the upper layer ( $b = 2^\circ$ ) being blue-shifted with respect to the lower one ( $b$





**Figure 5.** Intensity-weighted centroid velocity map of  $^{12}\text{CO}$  emission in the velocity range between  $-45$  and  $-8 \text{ km s}^{-1}$ .



**Figure 6.** H I integrated intensity map overlaid with the contours of  $^{12}\text{CO}$  emission in the Perseus arm. The integrated velocity range is from  $-45$  to  $8 \text{ km s}^{-1}$  for both H I and  $^{12}\text{CO}$ .

<sup>269</sup>  $= 0^\circ$ ). From the centroid velocity map, we can also see  
<sup>270</sup> that the lower layer runs up the Galactic plane gradu-

<sup>271</sup> ally from the west to the east, and then merges with the  
<sup>272</sup> upper layer at the position around  $[74, 2]^\circ$ .

As these two layers possess both good spatial and velocity coherence, we propose that they are two giant molecular filaments. Taking the distance of the Perseus arm to be 7.34 kpc (see Section 3.5 for the estimation of distance of each arm in this area), the lengths of these two giant molecular filaments are roughly 1.9 kpc, and their separation is roughly 0.12 kpc if we take their average Galactic latitude separation to be  $1^\circ$ .

To explore the possible origins of the two parallel filaments, we overlaid in Figure 6 the CO contours to the H I 21 cm line integrated intensity map over the same velocity range, from  $-45$  to  $-8$  km s $^{-1}$ . The H I data used in this work are obtained from the data release 2 of the Galactic Arecibo L-Band Feed Array H I (GALFA-H I) survey (Peek et al. 2018). The survey covers the region of  $0^{\text{h}} \leq \text{RA} \leq 24^{\text{h}}$  and  $-1^\circ 17' \leq \text{Dec} \leq +37^\circ 57'$ , i.e., 32% of the sky. The angular resolution is  $4'$  and the velocity resolution is 0.184 km s $^{-1}$ . The median rms noise is 352 mK per channel. From Figure 6, we can see that, overall, the molecular gas distribution correlates well with that of the H I gas. The H I gas shows a series of cavities between the two parallel giant molecular filaments which have sizes comparable to the separation of the filaments. This fact suggests that the H I gas cavities may be super bubbles and the two parallel giant molecular filaments may be caused by the compression of the super bubbles, with the upper filament representing the near-side layer of compressed molecular gas

and the lower filament being the far-side one. Surely, more observations of this region, such as radio continuum and OB star clusters, are needed to support this scenario.

### 3.4. Detection of Isotopologues in Different Arms

In the G60 region, the molecular gas in different arms can be further divided into three types of masks, according to the detection of  $^{12}\text{CO}$ ,  $^{13}\text{CO}$ , and  $\text{C}^{18}\text{O}$ . The regions with  $^{12}\text{CO}$  detection are defined as Mask 1, and the regions with both  $^{12}\text{CO}$  and  $^{13}\text{CO}$  detection are defined as Mask 2, while the regions with all three isotopologues being detected are defined as Mask 3. This means that the Mask 1 region contains Masks 2 and 3 regions, and the Mask 2 regions contain Mask 3 regions. The spatial distributions of Masks 1–3 in the four velocity ranges are shown in Figure 7, with Mask 1–3 regions in blue, green, and red colors, respectively.  $^{12}\text{CO}$  and  $^{13}\text{CO}$  are detected in all spiral arms, while  $\text{C}^{18}\text{O}$  is only detected in a few pixels of the Local Spur and the Local arm. Table 1 lists the total number and percentages of the detection of the  $^{12}\text{CO}$ ,  $^{13}\text{CO}$ , and  $\text{C}^{18}\text{O}$  emission in different arms and different Masks.  $^{13}\text{CO}$  is detected among 26% pixels with  $^{12}\text{CO}$  detection in the Local Spur and Local arm together. This percentage is 20% for the Perseus arm, and 12% for the Outer arm. The  $\text{C}^{18}\text{O}$  emission is detected among only about 0.27% pixels with  $^{12}\text{CO}$  detection in the Local Spur and Local arm together.

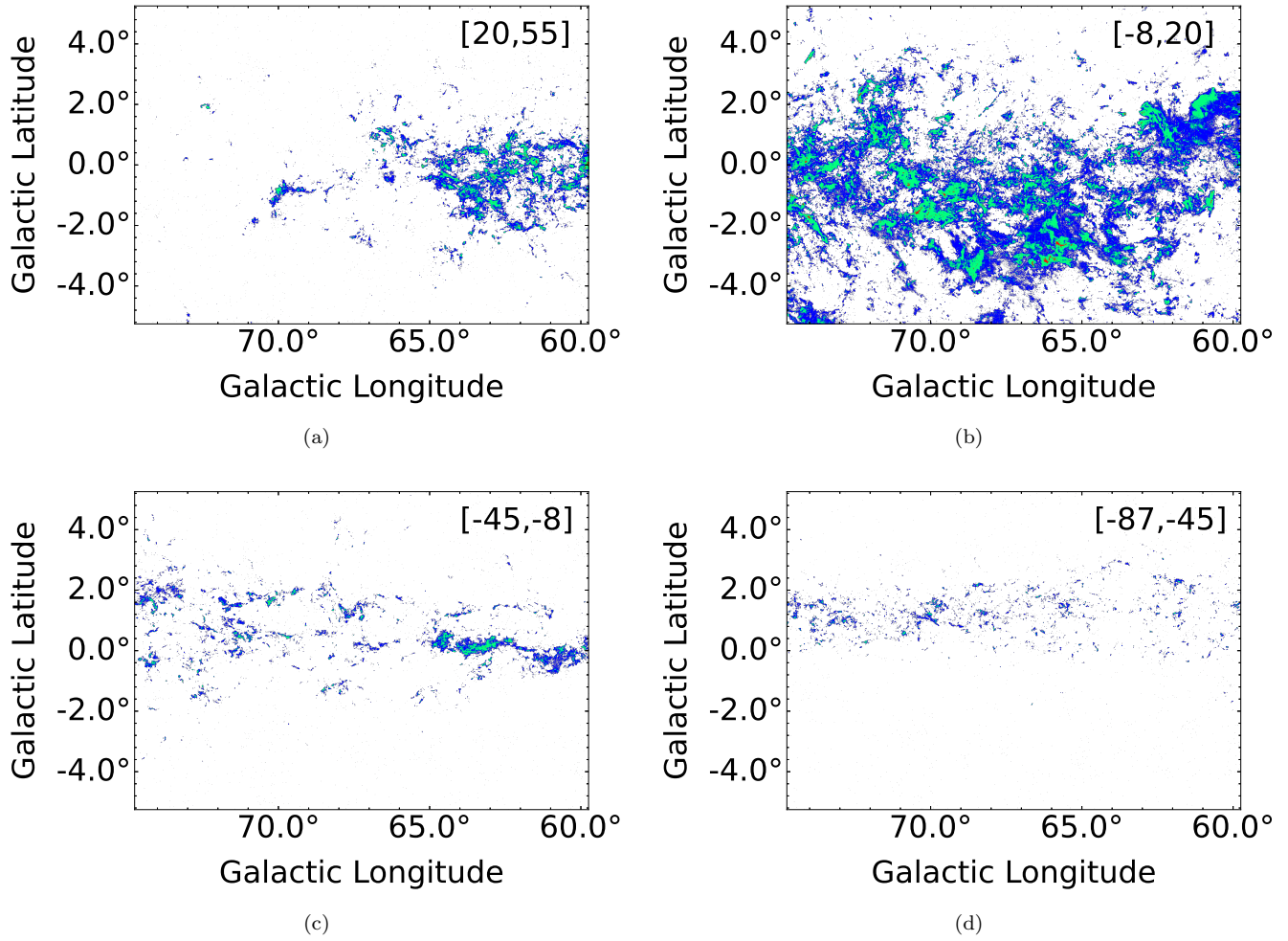


**Figure 7.** Spatial distributions of  $^{12}\text{CO}$ ,  $^{13}\text{CO}$ , and  $\text{C}^{18}\text{O}$  emission in four velocity ranges. The blue, green, and red colors indicate the regions where  $^{12}\text{CO}$ ,  $^{13}\text{CO}$ , and  $\text{C}^{18}\text{O}$  emission is detected, respectively. The (a) to (d) panels correspond to the Local Spur, Local, Perseus, and Outer arms, respectively. The velocity range of each arm is given in the top right corner of each panel.

Table 1. Statistical Properties of Molecular Gas in Different Spiral Arms of the G60 Region

Arm Name	Velocity Range ( $\text{km s}^{-1}$ )	Mask Name	Pixel Numer(per) %	Area ( $\text{deg}^2$ )	$T_{\text{ex}}$ (K)	$\tau_{13\text{CO}}$	$\tau_{\text{C}18\text{O}}$	$\log(N_{12\text{CO}})$ ( $\text{cm}^{-2}$ )	$\log(N_{13\text{CO}})$ ( $\text{cm}^{-2}$ )	$\log(N_{\text{C}18\text{O}})$ ( $\text{cm}^{-2}$ )
Local Spur	[20,55]	Mask 1	684890(30.15)	47.56	3.7–38.8(6.8)	...	...	15.46–18.32(17.09)	...	...
		Mask 2	181702 (8.00)	12.61	4.1–38.8(8.6)	...	...	...	14.34–17.27(15.97)	...
		Mask 3	1868 ( 0.08)	0.13	4.1–38.8(12.6)	0.07–8.61(0.31)	...	...	...	...
Local Arm	[–8,20]	Masks 1	124950 ( 5.50)	8.67	3.7–47.6(6.7)	...	0.02–1.35(0.14)	...	...	14.00–15.75(14.71)
		Mask 2	33028 (1.45)	2.29	4.1–47.6(8.8)	0.07–3.26(0.31)	...	15.46–18.57(17.05)	...	...
		Mask 3	345 (0.015)	0.02	5.2–47.6(13.8)	...	0.02–0.72(0.13)	...	13.97–17.76(15.99)	...
Perseus Arm	[–45,–8]	Mask 1	73867 (3.25)	5.13	3.8–31.9(6.1)	...	...	15.46–18.69(16.95)	...	14.01–15.9(14.79)
		Mask 2	14548 (0.64)	1.01	4.2–31.9(7.5)	...	...	...	...	...
		Mask 3	53(0.002)	...	5.3–29.9(10.1)	0.10–1.8(0.33)	...	...	14.06–17.7(15.87)	...
Outer Arm	[–87,–45]	Mask 1	31860(1.4)	2.21	3.6–22.0(5.9)	...	0.04–0.76(0.19)	15.46–18.04(16.84)	...	14.03–15.73(14.55)
		Mask 2	3925 (0.17)	0.27	4.1–22.0(7.5)	0.10–1.07(0.30)	...	...	14.02–16.9(15.75)	...
		Mask 3	22 (0.001)	...	5.1–7.3(6.6)	...	0.16–0.46(0.29)	...	...	...

NOTE—Columns 1–3: name of the arms, arm velocity range, and mask name (see Section 3.1). Columns 4–5: number of pixels with detection and detection percentage. Column 6, range and the median value (in parenthesis) of the excitation temperature. Columns 7–8: ranges and median values (in parenthesis) of the optical depths of  $^{13}\text{CO}$  and  $\text{C}^{18}\text{O}$  emission, respectively. Columns 9–11: ranges and median values (in parenthesis) of the column density of  $^{12}\text{CO}$ ,  $^{13}\text{CO}$ , and  $\text{C}^{18}\text{O}$ , respectively.

### 3.5. Statistical Properties of Molecular Gas in Different Spiral Arms

The distance of a molecular cloud is essential to estimate the physical parameters of the cloud. For molecular clouds located at relatively large distances ( $d > 3$  kpc), the distances of the individual clouds can be appropriately determined using the Galactic rotation curve and the radial velocities of the individual clouds (e.g. Ma et al. 2021). For molecular clouds located at relatively near distances, the above method may introduce large relative errors in the obtained distances. For these clouds, the extinction map can be used to derive reliable distances for the individual clouds (e.g. Zucker et al. 2019; Ma et al. 2021). In this work, we just attempt to estimate the statistical properties of molecular gas in different spiral arms. For this purpose, we do not try to determine the distances of individual clouds in each spiral arm, but use the measured parallaxes of masers located in each arm from the BeSSel survey as the reference distance to the molecular gas in each spiral arm. The association between the molecular gas and the masers is determined from the position-position-velocity information of the MWISP spectra and that of the masers. We assigned the mean parallax distance of masers in a spiral arm. Finally, the reference distances for the Local Spur, Local, Perseus, and Outer arms in the section within the Galactic longitudes studied in this work are 3.15, 3.01, 7.34, and 13.33 kpc, respectively.

With the reference distances, we can estimate the total mass of molecular hydrogen in each spiral arm. The total mass can be estimated through the summation of  $H_2$  column densities according to Eq. 1,

$$M = \mu m_H D^2 \int N_{H_2} d\Omega, \quad (1)$$

where  $N_{H_2}$  is the column density of molecular hydrogen,  $D$  is the distance,  $m_H$  is the mass of the hydrogen atom,  $\Omega$  is the total angular area the emission occupies, and  $\mu = 2.8$  is the mean molecular weight. The pixel-by-pixel  $N_{H_2}$  for each spiral arm can be calculated from the integrated  $^{12}CO$  intensity using the “ $X_{CO}$ ” method or from the integrated  $^{13}CO$  intensity using the “LTE” method, as introduced in Ma et al. (2021). We use  $X_{CO} = 2.0 \times 10^{20} \text{ cm}^{-2} (\text{K km s}^{-1})^{-1}$  (Bolatto et al. 2013) to convert the integrated intensity of  $^{12}CO$  emission into the  $H_2$  column density. Finally, the mass derived for the Local Spur, Local arm, Perseus arm, and Outer arms is  $1.02 \times 10^6$ ,  $5.29 \times 10^6$ ,  $2.63 \times 10^6$ , and  $2.75 \times 10^6 M_\odot$ , respectively, using the “ $X_{CO}$ ” method, while the mass is  $2.28 \times 10^5$ ,  $9.40 \times 10^5$ ,  $3.21 \times 10^5$ , and  $2.24 \times 10^5 M_\odot$ , respectively, using the LTE method.

Calculation of the excitation temperature, optical depth of the  $^{13}CO$  and  $C^{18}O$  emission, column density of the  $^{12}CO$ ,  $^{13}CO$ , and  $C^{18}O$  line emission for each pixel in Masks 1–3 in different spiral arms are the same as in Ma et al. (2021). The statistics of the above physical quantities are presented in Table 1 and Figure 8. For all the spiral arms, the Masks 1–2 regions have similar median  $T_{ex}$  of  $\sim 6$ –8 K, while the median  $T_{ex}$  is higher in the Mask 3 region, which is around 10–14 K. Statistically, the Perseus and Outer arms contain relatively higher fractions of pixels with  $T_{ex}$  higher than  $\sim 7$  K (see Figure 8 (a)). The  $^{13}CO$  emission is relatively optically thin, with median  $\tau_{^{13}CO}$  around 0.3, in all spiral arms, though there are pixels with  $^{13}CO$  optical depth up to 1.5. The  $C^{18}O$  emission is optically thin in all spiral arms, although  $\tau_{C^{18}O}$  can be up to 1.35 in some pixels.

The column densities of  $^{12}CO$  and  $^{13}CO$  in different arms have similar distributions, as shown in Figures 8 (d) and (e). The median column densities of  $^{12}CO$  in the Local Spur and Local arm are greater than that found in the Perseus and Outer arm by a factor of  $\sim 1.5$ . For  $C^{18}O$ , its median column density in the Local Spur is almost the same as that in the Local arm. We also present in Figure 18 the distributions of  $^{12}CO$  and  $^{13}CO$  column densities in the Appendix for each arm individually in the log-log space and the log-normal functions with parameters estimated from the data are overlaid. Log-normal distribution functions of column density (i.e., LN N-PDFs) usually indicate turbulence dominance in molecular gas (Kritsuk et al. 2010; Federrath & Klessen 2013), while excesses from LN distributions imply self-gravity dominance, and they typically coincide to star formation activities (Kainulainen et al. 2009). In our results, the N-PDFs of  $^{12}CO$  emission in the Local Spur, Local arm, and Outer arm are well described by LN functions, while that of the Perseus arm has a slight excess at the high column density end. In contrast, the  $^{13}CO$  N-PDFs for the Local Spur and the Perseus arm have significant excesses above LN distribution at their high column density ends. The regions in the Local spur and the Perseus arm where the  $^{13}CO$  column density exceeds the value at which significant excess above LN distribution appears are indicated with orange boxes in Figure 13 (a) and (c). As shown in Figure 13 (a) for Local spur, four regions have high column density, among which three hosts H II regions (G060.873-00.108, G061.473+00.094) or maser ( $l = 59.78^\circ$ ,  $b = 0.06^\circ$ ). For the Perseus arm in Figure 13 (c), one region possesses high column density and it hosts a maser ( $l = 70.18^\circ$ ,  $b = 1.74^\circ$ ). Therefore, we can see that the majority of the high-column density regions host ongoing star formation.

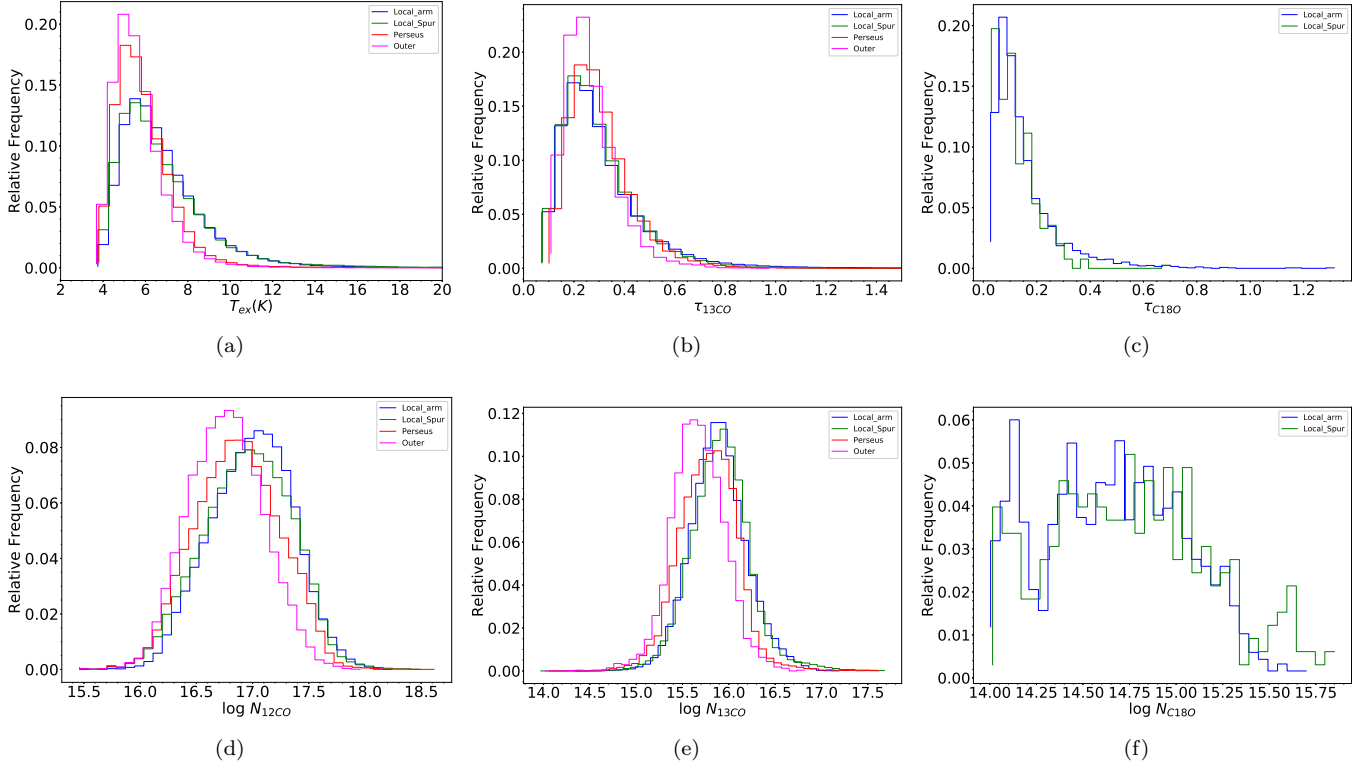


**Figure 8.** Histograms of excitation temperature in Mask 1 regions (a), optical depth of  $^{13}\text{CO}$  in Mask 2 regions (b), optical depth of  $\text{C}^{18}\text{O}$  in Mask 3 regions (c), column density of  $^{12}\text{CO}$  in Mask 1 regions (d), column density of  $^{13}\text{CO}$  in Mask 2 regions (e), column density of  $\text{C}^{18}\text{O}$  in Mask 3 regions (f) in different spiral arms. Different colors represent different spiral arms.

### 3.6. Clouds in the Outer-Scutum-Centaurus Arm

Benefitting from the high sensitivity of the MWISP survey, we could try to identify distant molecular clouds in the Galactic plane. From the  $^{12}\text{CO}$  line emission data, we identified 15 extremely  $^{12}\text{CO}$  clouds within kinematic distances of  $\sim[14.72, 17.77]$  kpc using the algorithm of Density-Based Spatial Clustering of Applications with Noise (DBSCAN; Ester et al. 1996). Before the identification, the  $^{12}\text{CO}$  data are masked above  $2\sigma_{\text{RMS}}$ , which is the standard criterion used in a series of works of the MWISP project (e.g., Yan et al. 2020; Ma et al. 2022; Yuan et al. 2022). The DBSCAN algorithm has two input parameters, i.e.,  $\epsilon$  and  $\text{MinPts}$ . We used the set of parameters  $\epsilon = 1$  and  $\text{MinPts} = 4$  in this work. This settings of the parameters are adopted from Yan et al. (2020), which are found most suitable for the MWISP data. The definitions of the two parameters have also been explained in detail in Yan et al. (2020) and Ma et al. (2022). Figure 9 displays the integrated-intensity maps and average spectra of three of these molecular clouds as an example. The identified molecular clouds are outlined with red lines in Figures 9 (a1), (b1), and (c1). The spectra in Figures 9 (a2), (b2), and (c2) are averaged within the outlines of the clouds. The two

vertical dash lines in Figures 9 (a2), (b2), and (c2) represent the velocity spans of the corresponding clouds. Similar maps and spectra for the other 12 extremely distant clouds are given in Figure 19 in the Appendix.

For the distances of these clouds, we adopt their kinematic distances assuming a flat Galactic rotation curve, a solar Galactocentric distance  $R_0 = 8.15$  kpc, and a circular velocity of the Sun of  $\Theta_0 = 236 \text{ km s}^{-1}$  (Reid et al. 2019). The kinematic distances of these clouds range from 14.72 kpc to 17.77 kpc. We use the  $X_{\text{CO}}$  factor to convert the integrated intensity of  $^{12}\text{CO}$  emission into the  $\text{H}_2$  column density of clouds, and then calculate their mass according to Eq. 1. The mass of these molecular clouds ranges from 363 to 520  $M_{\odot}$ . The centroid velocity, distance, and mass are tabulated in Table 2.

Combining H I data and the MWISP data, Sun et al. (2015) identified 72 clouds with masses of  $10^2$ - $10^4 M_{\odot}$  within Galactocentric radii of 15 to 19 kpc, which they found are likely to be the extension of the arm identified by Dame & Thaddeus (2011). This portion of the arm could be the extension of Scutum-Centaurus arm into the outer Galaxy. We overlaid the molecular clouds from Dame & Thaddeus (2011), the molecular clouds identified in this work and in Sun et al. (2015) that are associated with the OSC arm in an artist's conception

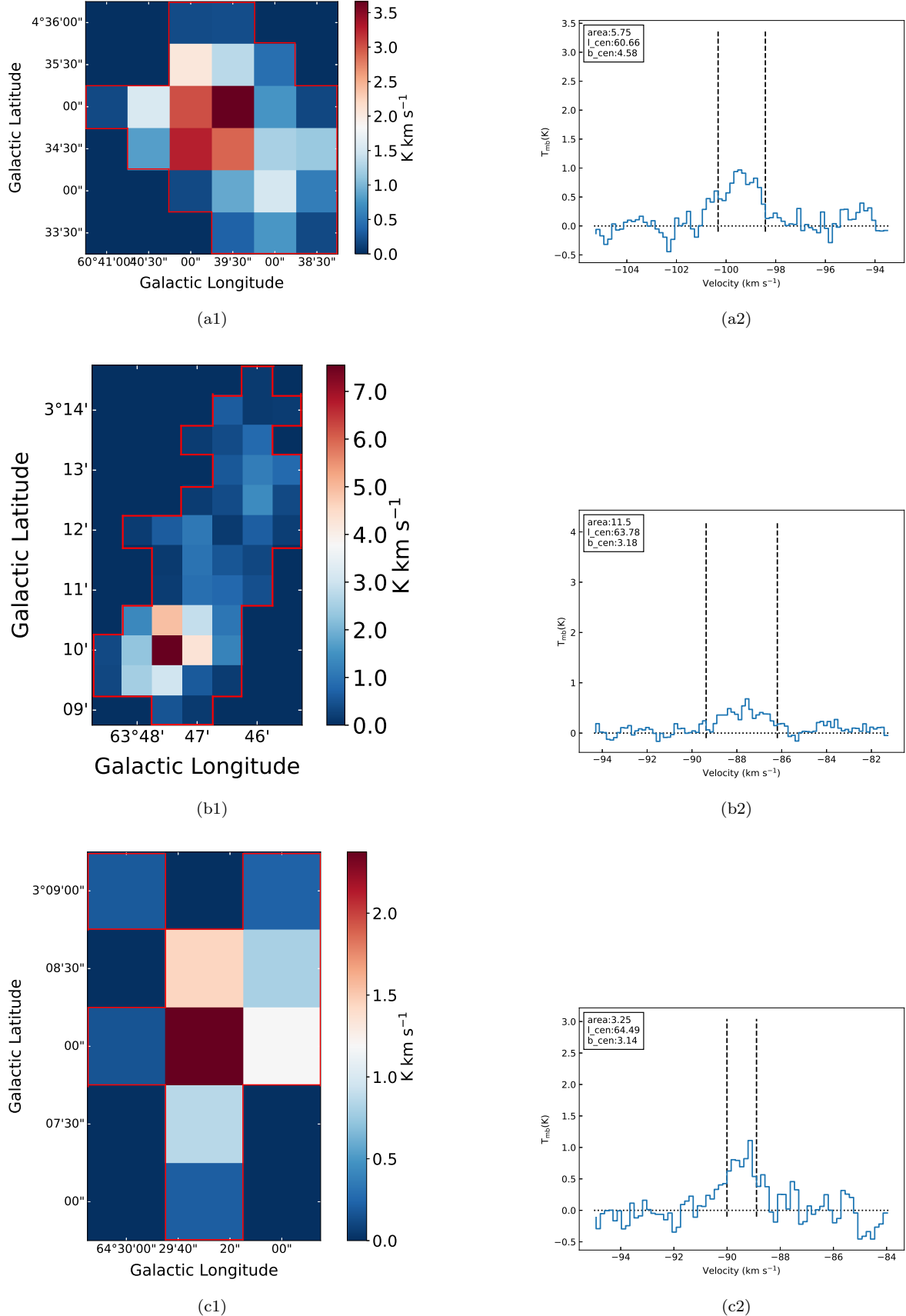


**Figure 9.** Integrated intensity maps (a1, b1, and c1) and average spectra (a2, b2, and c2) of three distant clouds. The red outlines represent the boundaries of molecular clouds. Two vertical dashed lines in each average spectrum indicate the velocity range of the cloud. The angular sizes in units of arcmin<sup>2</sup> and the coordinates of the clouds in degrees are indicated in the top-left corner of the average spectra.

of the Milky Way<sup>3</sup> in Figure 10. The locations of the molecular clouds identified by Dame & Thaddeus (2011) and the molecular clouds identified by Sun et al. (2015) are indicated with yellow circles and red circles, respectively. The green circles represent the distant molecular clouds identified in this work. We also overlaid the best fitting of the new arm identified by Dame & Thaddeus (2011) and Sun et al. (2015) in Figure 10. The spiral arm parameters, such as the pitch angle and the reference Galactocentric azimuth, are adopted from Sun et al. (2015). The distribution of the distant molecular clouds that we identified in this work can reasonably be thought to follow the best-fitting curve of the OSC arm. Therefore, these 15 distant molecular clouds probably trace the extension of the OSC arm within the Galactic longitude from 60° to 75°. However, we note that only three of these 15 molecular clouds are located near the best-fitting curve of the OSC arm, while the other 12 molecular clouds are located in the middle between the Outer and the OSC arms. These 12 molecular clouds constitute a nearly linear filament, which may be an independent structure or a spur, rather than part of an arm, such as the newly discovered Cattail giant H I filament, which is located between the Galactic longitude from 80 to 95° and well beyond the OSC arm (Li et al. 2021).

#### 4. DISCUSSION: VERTICAL DISTRIBUTION

Early H I surveys have found that the Galactic plane of H I gas warps upward above the  $b = 0^\circ$  plane for the Galactocentric azimuth range  $0^\circ \leq l \leq 180^\circ$  and downward below the  $b = 0^\circ$  plane for the range of  $180^\circ \leq l \leq 360^\circ$  (Westerhout 1957; Henderson et al. 1982; Burton 1988). Surveys of molecular gas have shown that the flaring and warping of the molecular gas layer in the outer Galactic varies strongly with Galactocentric azimuth and exhibits a similar structure with that of the H I gas layer (Clemens et al. 1988; Wouterloot et al. 1990). Using the CO ( $J = 1-0$ ) data from the CfA-Chile survey, Nakanishi & Sofue (2006) found that the thickness of the molecular gas disk increases from 48 to 90 pc within the solar circle and then abruptly increases at a Galactocentric radius of 11 kpc. They also found that the molecular gas disk also shows warping above the Galactic mid-plane in the outer Galaxy within the azimuth angles from 60° to 140°. With the high-sensitivity CO data from MWISP, we have the chance to analyze the vertical distribution of molecular gas in the section of the Galactic plane studied in this work.

We calculated the total mass within each 20 pc bin perpendicular to the Galactic plane. The vertical height of each bin is derived through  $z = d \sin(b)$ , where  $d$  is the distance to the Sun of the molecular gas and  $b$  is the central Galactic latitude of the bin. Here, the distances estimated for each arm in Section 3.5 are adopted. Figure 11 (a) and (b) show the vertical distribution of gas mass in Mask 1 estimated from <sup>12</sup>CO emission using the X<sub>CO</sub> factor method and that in Mask 2 from <sup>13</sup>CO emission using the LTE method for different arms, respectively. The red, green, blue, and magenta histograms represent the gas in the Local Spur, Local arm, Perseus arm, and Outer arm, respectively. From Figures 11 (a) and 11 (b), we can see that the molecular gas in the Local spur and Local arm are generally concentrated around the Galactic mid-plane, with the molecular gas in the Local arm slightly displaced below  $z = 0$  pc. The molecular gas in the Perseus arm is distributed mainly around  $z = 0$  and  $z = 200$  pc. A large positive displacement exists for the molecular gas in the Outer arm, which is quite consistent with the warping feature identified by Nakanishi & Sofue (2006). In the G60 region, the warp starts at a distance between the Perseus arm and the Outer arm.

For quantitative description, we also fit the vertical mass distributions in each arm with Gaussian functions, and the results are given in Figures 11 (c)–(f) for <sup>12</sup>CO emission (Mask 1), and Figures 11 (g)–(j) for <sup>13</sup>CO emission (Mask 2), respectively. For suitable fittings the bin widths in Figures 11 (c)–11 (j) have been adjusted to the appropriate values. The thickness of the molecular gas layer does not increase monotonically with the distances of the molecular gas. At similar distances, the molecular gas in the Local arm has an FWHM of 243 pc measured from the <sup>12</sup>CO emission, which is about 2.5 times that in the Local Spur. The FWHM thickness of the <sup>13</sup>CO gas in the Local arm is 216 pc and its ratio to the thickness of the Local Spur is slightly higher than that obtained from <sup>12</sup>CO emission. The vertical distribution of molecular gas in the Perseus arm can be well-fitted with two components of Gaussian functions. Combined with the spatial distribution of molecular gas in Figures 4 and 7, the two Gaussian components correspond to two giant filaments parallel to the Galactic plane. The two Gaussian components have a vertical distance of  $\sim 190$  and 186 pc as seen from the <sup>12</sup>CO and <sup>13</sup>CO emission, respectively. The FWHM thickness of the  $z \sim 200$  pc component obtained from the <sup>13</sup>CO emission is much smaller than that obtained from the <sup>12</sup>CO emission. This feature of two parallel components in the G60 section of the Milky Way is first observed in this work. At the distance of  $\sim 13$  kpc, the thickness of

<sup>3</sup> R.Hurt: NASA/JPL-Caltech/SSC



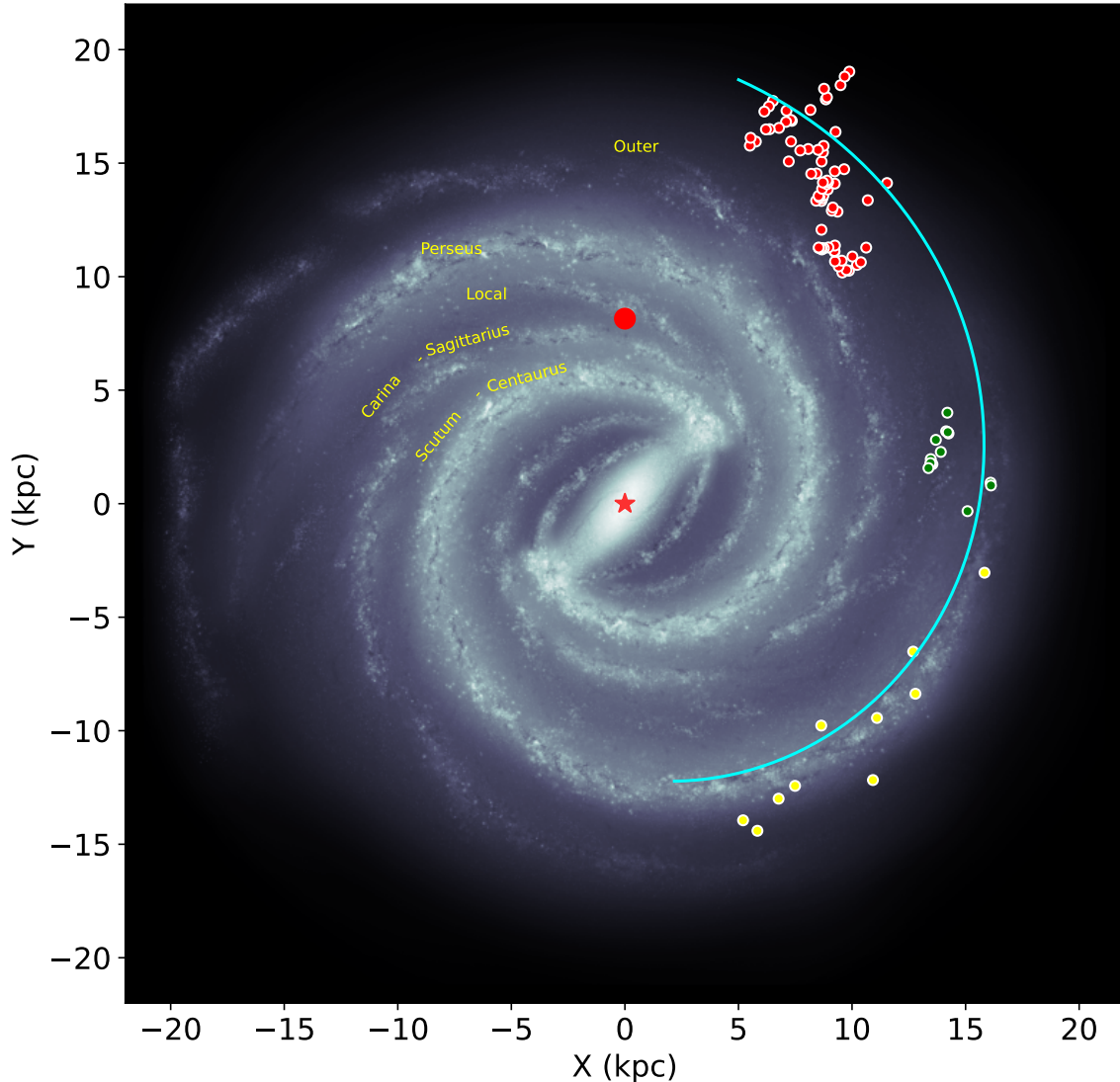


**Figure 10.** Locations of molecular clouds in the OSC arm superposed on the artist’s conception of the Milky Way (R.Hurt: NASA/JPL-Caltech/SSC). The green circles, yellow circles, and red circles indicate clouds covering Galactic longitudes from  $l = 59.75^\circ$  to  $74.75^\circ$  detected in this work,  $l = 13^\circ$  to  $55^\circ$  detected by Dame & Thaddeus (2011), and  $l = 100^\circ$  to  $150^\circ$  detected by Sun et al. (2015). The cyan dashed line is a logarithmic spiral line fit to the Scutum-Centaurus arm. (Reid et al. 2019). The Galactic center is marked with a star symbol and the location of the Sun is marked with a large red dot.

579 the Outer arm gas is about 265 pc. Along the direc-  
 580 tions of  $l = 60-75^\circ$ , the distances 13 kpc corresponds  
 581 to Galactocentric distance of 11.3–13.4 kpc. Therefore,  
 582 the thickness of the Outer arm that we obtained is 1.6  
 583 times the thickness of the molecular disk found by in  
 584 Nakanishi & Sofue (2006) at a comparable Galactocen-  
 585 tric radius. From Figures 11 (f) and (j), we can see that  
 586 the molecular gas disk at the Galactocentric distances  
 587 of 11.3–13.4 kpc, as traced by the Outer arm, warps  
 588 upward with respect to the  $b = 0^\circ$  plane with an ampli-  
 589 tude of 273 pc from the  $^{12}\text{CO}$  emission, which is similar  
 590 to that (258 pc) from  $^{13}\text{CO}$  emission.

## 5. SUMMARY

591  
 592 Using the multi-line MWISP survey data, we per-  
 593 formed a comprehensive study of the physical properties  
 594 of the molecular gas in the range of  $l = 59.75^\circ \sim 74.75^\circ$   
 595 and  $b = -5.25^\circ \sim 5.25^\circ$ . The large-scale distribution of  
 596 the molecular gas is presented. We used the DBSCAN  
 597 algorithm to identify molecular clouds traced by  $^{12}\text{CO}$   
 598 emission in the velocity range of  $-119 \sim -87 \text{ km s}^{-1}$ .  
 599 We analysed the vertical distribution of the molecular

**Table 2.** Parameters of Molecular Clouds in the OSC Arm

Number	l	b	$V_{\text{lsr}}$	$T_{\text{peak}}$	Area	d	Mass
	( $^{\circ}$ )	( $^{\circ}$ )	( $\text{km s}^{-1}$ )	(K)	( $\text{arcmin}^2$ )	(kpc)	( $M_{\odot}$ )
(1)	(2)	(3)	(4)	(5)	(6)	(7)	(8)
1	60.66	4.58	-99.35	3.25	5.75	17.36	497
2	63.78	3.18	-87.7	4.11	11.50	14.92	367
3	64.49	3.14	-89.41	2.94	3.25	14.95	368
4	64.64	3.01	-89.46	2.38	5.00	14.92	367
5	64.67	2.88	-90.18	2.35	2.25	15.00	371
6	64.69	2.93	-89.37	2.26	3.75	14.90	366
7	65.32	2.94	-90.17	2.39	2.25	14.84	363
8	65.49	4.60	-110.94	2.93	3.50	17.77	520
9	65.83	4.78	-111.19	2.79	4.50	17.71	517
10	67.12	3.21	-95.87	2.80	4.50	15.12	377
11	68.70	3.31	-95.72	3.23	6.75	14.72	357
12	70.46	3.04	-102.14	3.38	14.00	15.14	378
13	70.62	2.94	-102.08	2.72	2.50	15.09	375
14	70.67	3.10	-101.57	4.33	7.25	15.01	371
15	73.73	3.07	-105.42	2.46	4.75	14.81	361

NOTE—Column 1: cloud number which is organized by increasing galactic longitude. Columns 2–6 give the centroid position, the centroid velocity, the peak intensity, and the angular area of the clouds. The distance and the mass of the clouds are presented in columns 7–8.

600 gas in this region. The main results of this study are  
601 presented as follows:

- 602 1. The molecular gas in the observed region can be  
603 attributed to one structure and three arms, i.e.,  
604 the Local spur, Local arm, Perseus arm, and Outer  
605 arm. We present the distribution and velocity  
606 structures of the molecular gas in this part of the  
607 Galactic plane in detail for the first time. De-  
608 tailed statistics of the properties of the molecular  
609 gas such as excitation temperature, optical depth,  
610 and column density are calculated for each arm  
611 and the Local spur.
- 612 2. We identified 15 extremely distant molecular  
613 clouds with kinematic distances of 14.72–17.77  
614 kpc and masses of 363–520  $M_{\odot}$ , which we find  
615 could be part of the Scutum-Centaurus arm in  
616 the outer Galaxy identified by [Dame & Thaddeus](#)  
617 [\(2011\)](#) and [Sun et al. \(2015\)](#). There is also a  
618 possibility that 12 of these extremely molecular  
619 clouds may be an independent structure between  
620 the Outer and the OSC arms, or a spur.
- 621 3. We observed a warp for the molecular gas in the  
622 Outer spiral arm and a two-component distribu-  
623 tion of the molecular gas in the Perseus spiral arm.  
624 The two Gaussian components in the vertical dis-  
625 tribution of the molecular gas in the Perseus arm  
626 in the G60 region are observed for the first time,  
627 and they correspond to two giant filaments parallel  
628 to the Galactic plane.

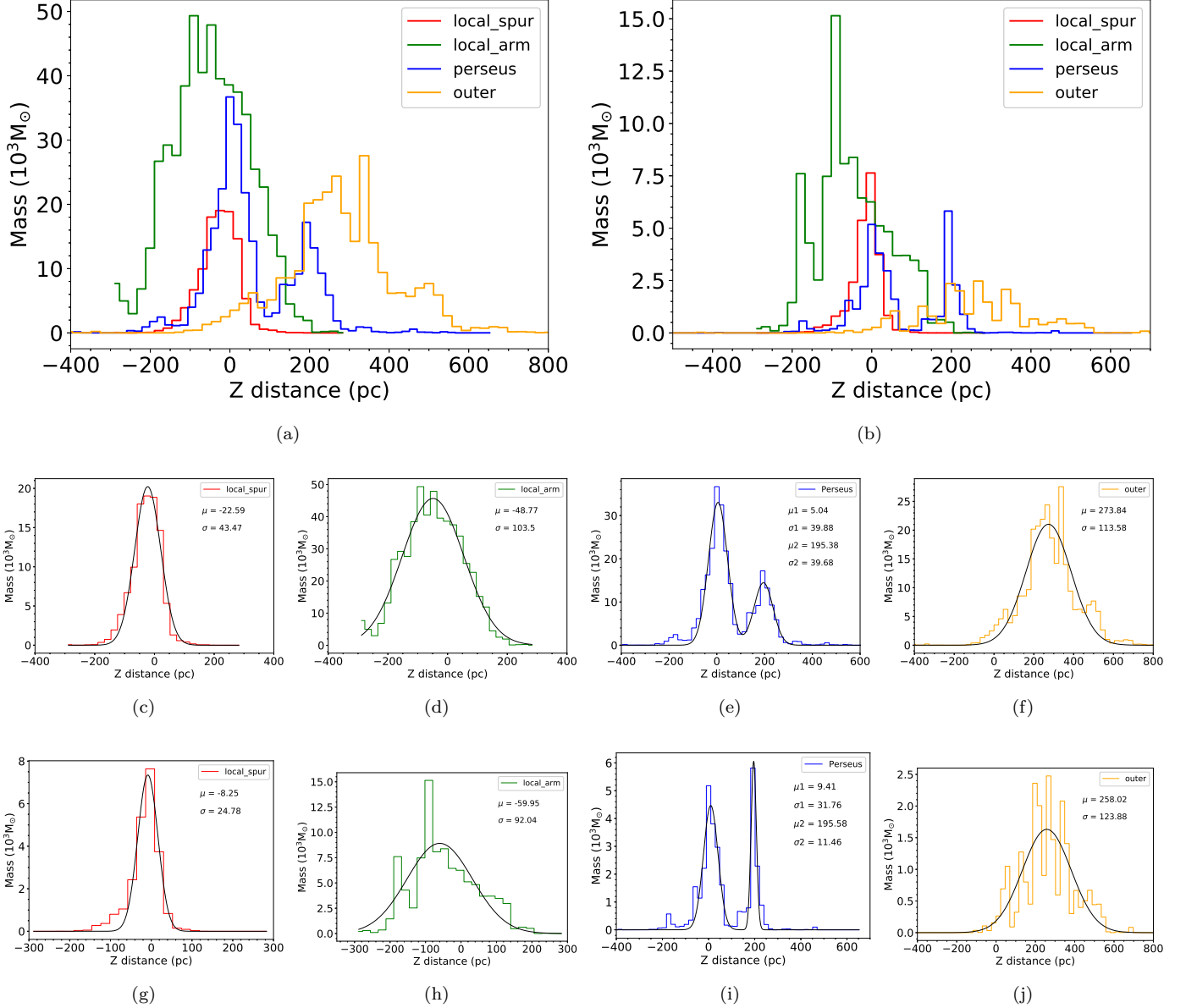


**Figure 11.** Mass distributions along the  $z$  direction for different spiral arms. The distributions for molecular gas in the mask 1 and mask 2 regions are presented in (a) and (b), respectively. The Gaussian fittings to the distributions of  $^{12}\text{CO}$  gas (mask 1) are shown in (c)-(f) and those of  $^{13}\text{CO}$  gas (mask 2) in (g)-(j). The fitted parameters,  $\mu$  and  $\sigma$ , are indicated in the top-right corners of the panels.

629 We thank the anonymous referee for the constructive  
 630 suggestions that helped to improve this manuscript.  
 631 This research made use of the data from the Milky Way  
 632 Imaging Scroll Painting (MWISP) project, which is a  
 633 multi-line survey in  $^{12}\text{CO}/^{13}\text{CO}/\text{C}^{18}\text{O}$  along the north-  
 634 ern Galactic plane with the PMO-13.7m telescope. We  
 635 are grateful to all the members of the MWISP working  
 636 group, particularly the staff members at PMO-13.7m  
 637 telescope, for their long-term support. MWISP was  
 638 sponsored by National Key R&D Program of China  
 639 with grant 2017YFA0402701 and CAS Key Research  
 640 Program of Frontier Sciences with grant QYZDJ-SSW-  
 641 SLH047. This publication utilizes the GALFA-H I sur-  
 642 vey data set obtained with the Arecibo L-band Feed  
 643 Array (ALFA) on the Arecibo 305 m telescope. The  
 644 Arecibo Observatory is operated by SRI International  
 645 under a cooperative agreement with the National Sci-  
 646 ence Foundation (AST-1100968), and in alliance with  
 647 Ana G. Méndez-Universidad Metropolitana and the  
 648 Universities Space Research Association. The GALFA-  
 649 H I surveys have been funded by the NSF through grants  
 650 to Columbia University, the University of Wisconsin,  
 651 and the University of California. We acknowledge the  
 652 support of NSFC grants 11973091 and 12173090. C.L.  
 653 acknowledges the supports by China Postdoctoral Sci-  
 654 ence Foundation No.2021M691532, and Jiangsu Post-  
 655 doctoral Research Funding Program No. 2021K179B.  
 656 Y.S. acknowledges support by the Youth Innovation  
 657 Promotion Association, CAS (Y2022085), and Light of  
 658 West China Program, CAS (2022-XBJCTD-003).

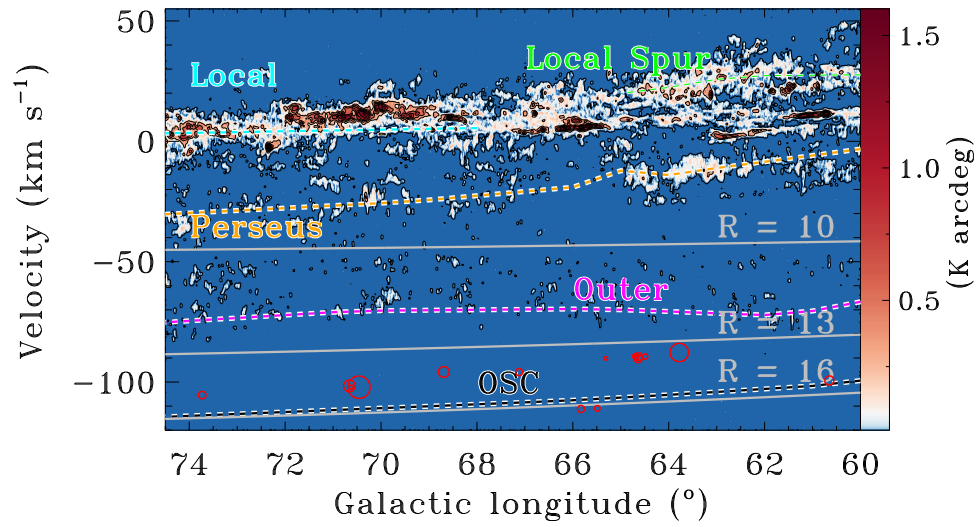
## REFERENCES

- 659 Anderson, L. D., Bania, T. M., Balsler, D. S., et al. 2014,  
 660 *ApJS*, 212, 1, doi: [10.1088/0067-0049/212/1/1](https://doi.org/10.1088/0067-0049/212/1/1)
- 661 Blitz, L. 1993, in *Protostars and Planets III*, ed. E. H. Levy  
 662 & J. I. Lunine, 125
- 663 Bolatto, A. D., Wolfire, M., & Leroy, A. K. 2013, *ARA&A*,  
 664 51, 207, doi: [10.1146/annurev-astro-082812-140944](https://doi.org/10.1146/annurev-astro-082812-140944)
- 665 Burton, W. B. 1988, in *Galactic and Extragalactic Radio*  
 666 *Astronomy*, ed. K. I. Kellermann & G. L. Verschuur,  
 667 295–358
- 668 Clemens, D. P., Sanders, D. B., & Scoville, N. Z. 1988,  
 669 *ApJ*, 327, 139, doi: [10.1086/166177](https://doi.org/10.1086/166177)
- 670 Dame, T. M., Hartmann, D., & Thaddeus, P. 2001, *ApJ*,  
 671 547, 792, doi: [10.1086/318388](https://doi.org/10.1086/318388)
- 672 Dame, T. M., & Thaddeus, P. 2011, *ApJL*, 734, L24,  
 673 doi: [10.1088/2041-8205/734/1/L24](https://doi.org/10.1088/2041-8205/734/1/L24)
- 674 Ester, M., Kriegel, H.-P., Sander, J., Xu, X., et al. 1996, in  
 675 *Kdd*, Vol. 96, 226–231
- 676 Federrath, C., & Klessen, R. S. 2013, *The Astrophysical*  
 677 *Journal*, 763, 51, doi: [10.1088/0004-637X/763/1/51](https://doi.org/10.1088/0004-637X/763/1/51)
- 678 Green, D. A. 2019, *Journal of Astrophysics and Astronomy*,  
 679 40, 36, doi: [10.1007/s12036-019-9601-6](https://doi.org/10.1007/s12036-019-9601-6)
- 680 Henderson, A. P., Jackson, P. D., & Kerr, F. J. 1982, *ApJ*,  
 681 263, 116, doi: [10.1086/160486](https://doi.org/10.1086/160486)
- 682 Heyer, M. H., Carpenter, J. M., & Snell, R. L. 2001, *ApJ*,  
 683 551, 852, doi: [10.1086/320218](https://doi.org/10.1086/320218)
- 684 Kainulainen, J., Beuther, H., Henning, T., & Plume, R.  
 685 2009, *A&A*, 508, L35, doi: [10.1051/0004-6361/200913605](https://doi.org/10.1051/0004-6361/200913605)
- 686 Kramer, C., Stutzki, J., Rohrig, R., & Corneliussen, U.  
 687 1998, *A&A*, 329, 249
- 688 Kritsuk, A. G., Norman, M. L., & Wagner, R. 2010, *The*  
 689 *Astrophysical Journal Letters*, 727, L20,  
 690 doi: [10.1088/2041-8205/727/1/L20](https://doi.org/10.1088/2041-8205/727/1/L20)
- 691 Larson, R. B. 1981, *MNRAS*, 194, 809,  
 692 doi: [10.1093/mnras/194.4.809](https://doi.org/10.1093/mnras/194.4.809)

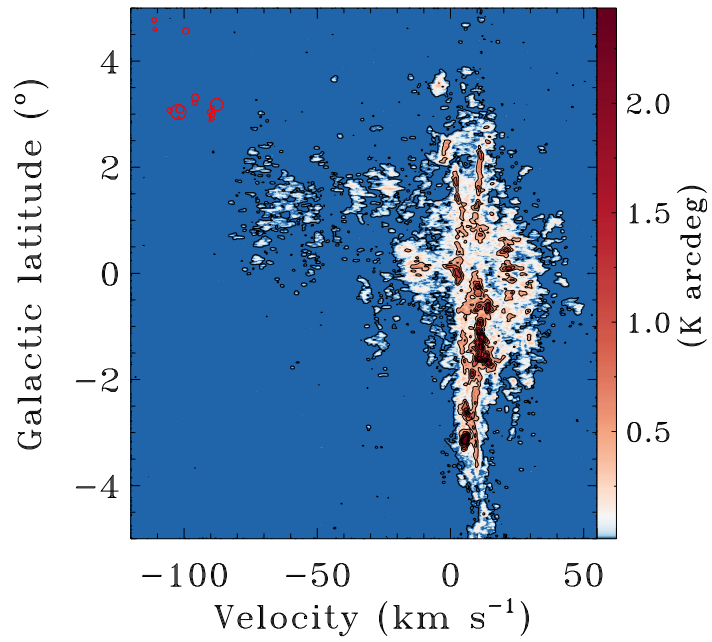
- 693 Li, C., Qiu, K., Hu, B., & Cao, Y. 2021, *ApJL*, 918, L2,  
694 doi: [10.3847/2041-8213/ac19bc](https://doi.org/10.3847/2041-8213/ac19bc)
- 695 Ma, Y., Wang, H., Li, C., et al. 2021, *ApJS*, 254, 3,  
696 doi: [10.3847/1538-4365/abe85c](https://doi.org/10.3847/1538-4365/abe85c)
- 697 Ma, Y., Wang, H., Zhang, M., et al. 2022, *ApJS*, 262, 16,  
698 doi: [10.3847/1538-4365/ac7797](https://doi.org/10.3847/1538-4365/ac7797)
- 699 Nakanishi, H., & Sofue, Y. 2006, *PASJ*, 58, 847,  
700 doi: [10.1093/pasj/58.5.847](https://doi.org/10.1093/pasj/58.5.847)
- 701 Peek, J. E. G., Babler, B. L., Zheng, Y., et al. 2018, *ApJS*,  
702 234, 2, doi: [10.3847/1538-4365/aa91d3](https://doi.org/10.3847/1538-4365/aa91d3)
- 703 Reid, M. J., Menten, K. M., Brunthaler, A., et al. 2019,  
704 *ApJ*, 885, 131, doi: [10.3847/1538-4357/ab4a11](https://doi.org/10.3847/1538-4357/ab4a11)
- 705 Rice, T. S., Goodman, A. A., Bergin, E. A., Beaumont, C.,  
706 & Dame, T. M. 2016, *ApJ*, 822, 52,  
707 doi: [10.3847/0004-637X/822/1/52](https://doi.org/10.3847/0004-637X/822/1/52)
- 708 Roman-Duval, J., Heyer, M., Brunt, C. M., et al. 2016,  
709 *ApJ*, 818, 144, doi: [10.3847/0004-637X/818/2/144](https://doi.org/10.3847/0004-637X/818/2/144)
- 710 Roman-Duval, J., Jackson, J. M., Heyer, M., Rathborne, J.,  
711 & Simon, R. 2010, *ApJ*, 723, 492,  
712 doi: [10.1088/0004-637X/723/1/492](https://doi.org/10.1088/0004-637X/723/1/492)
- 713 Schuller, F., Urquhart, J. S., Csengeri, T., et al. 2021,  
714 *MNRAS*, 500, 3064, doi: [10.1093/mnras/staa2369](https://doi.org/10.1093/mnras/staa2369)
- 715 Shan, W., Yang, J., Shi, S., et al. 2012, *IEEE Transactions*  
716 *on Terahertz Science and Technology*, 2, 593,  
717 doi: [10.1109/TTHZ.2012.2213818](https://doi.org/10.1109/TTHZ.2012.2213818)
- 718 Sharpless, S. 1959, *ApJS*, 4, 257, doi: [10.1086/190049](https://doi.org/10.1086/190049)
- 719 Solomon, P. M., Rivolo, A. R., Barrett, J., & Yahil, A.  
720 1987, *ApJ*, 319, 730, doi: [10.1086/165493](https://doi.org/10.1086/165493)
- 721 Su, Y., Yang, J., Zhang, S., et al. 2019, *ApJS*, 240, 9,  
722 doi: [10.3847/1538-4365/aaf1c8](https://doi.org/10.3847/1538-4365/aaf1c8)
- 723 Sun, Y., Xu, Y., Yang, J., et al. 2015, *ApJL*, 798, L27,  
724 doi: [10.1088/2041-8205/798/2/L27](https://doi.org/10.1088/2041-8205/798/2/L27)
- 725 Umemoto, T., Minamidani, T., Kuno, N., et al. 2017,  
726 *PASJ*, 69, 78, doi: [10.1093/pasj/psx061](https://doi.org/10.1093/pasj/psx061)
- 727 Westerhout, G. 1957, *BAN*, 13, 201
- 728 Wilson, R. W., Jefferts, K. B., & Penzias, A. A. 1970,  
729 *ApJL*, 161, L43, doi: [10.1086/180567](https://doi.org/10.1086/180567)
- 730 Wouterloot, J. G. A., Brand, J., Burton, W. B., & Kwee,  
731 K. K. 1990, *A&A*, 230, 21
- 732 Yan, Q.-Z., Yang, J., Su, Y., Sun, Y., & Wang, C. 2020,  
733 *The Astrophysical Journal*, 898, 80,  
734 doi: [10.3847/1538-4357/ab9f9c](https://doi.org/10.3847/1538-4357/ab9f9c)
- 735 Yuan, L., Yang, J., Du, F., et al. 2022, arXiv e-prints,  
736 arXiv:2212.02066. <https://arxiv.org/abs/2212.02066>
- 737 Zucker, C., Speagle, J. S., Schlafly, E. F., et al. 2019, *ApJ*,  
738 879, 125, doi: [10.3847/1538-4357/ab2388](https://doi.org/10.3847/1538-4357/ab2388)

## APPENDIX

740 The position-velocity diagrams and the integrated intensity maps of the  $^{13}\text{CO}$  line emission are presented in Figure  
741 12 and 13. The velocity channel maps of the  $^{12}\text{CO}$  line emission in each spiral arm and Local Spur are presented in  
742 Figures 14, 15, 16, and 17. Figure 18 presents the distributions of  $^{12}\text{CO}$  and  $^{13}\text{CO}$  column densities for each arm and  
743 the fittings with log-normal function are overlaid. Figure 19 is similar to Figure 9, but for the other 12 extremely  
744 distant molecular clouds.

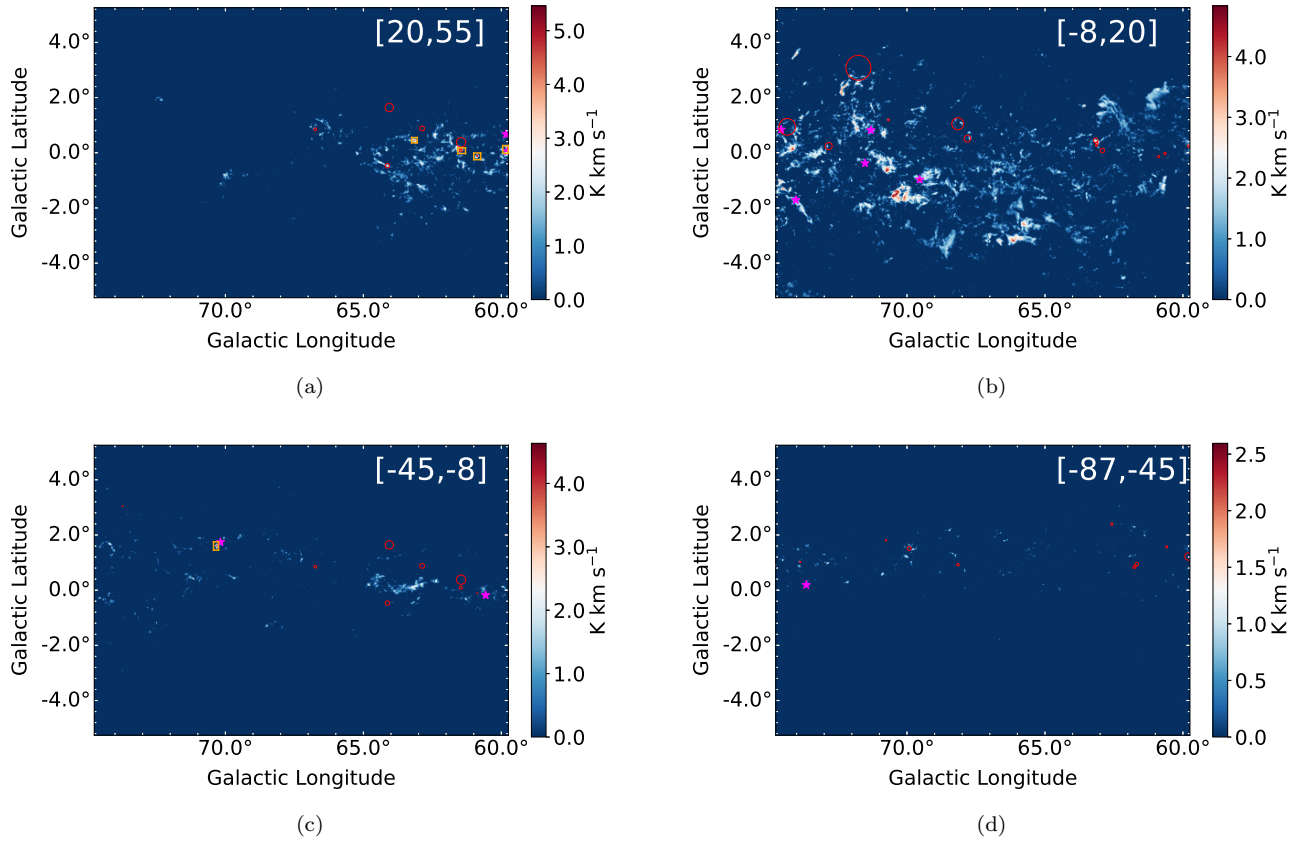


(a)



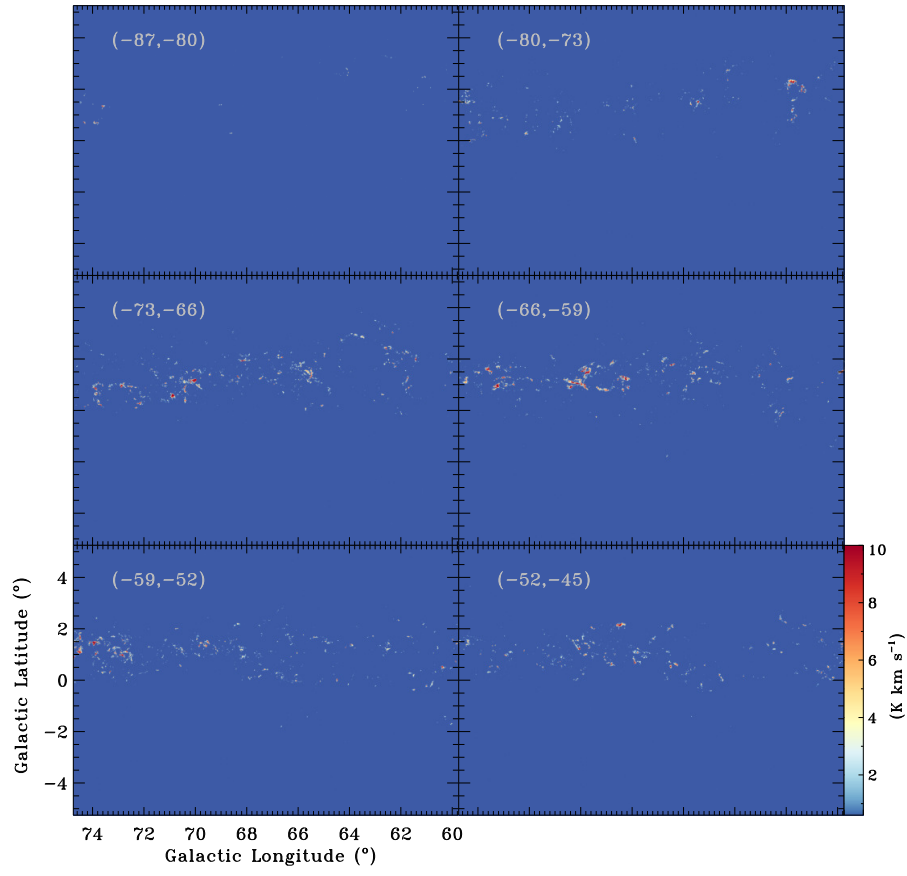
(b)

Figure 12. Same as Figure 2 but for  $^{13}\text{CO}$  line emission.



**Figure 13.** Same as Figure 4 but for  $^{13}\text{CO}$  line emission. The orange boxes in (a) and (c) mark the regions with high-column density.





**Figure 14.** Velocity channel maps of  $^{12}\text{CO}$  from  $-87$  to  $-45$   $\text{km s}^{-1}$  of the Outer arm. The velocity range of each channel is shown at the top-left corner of each panel.

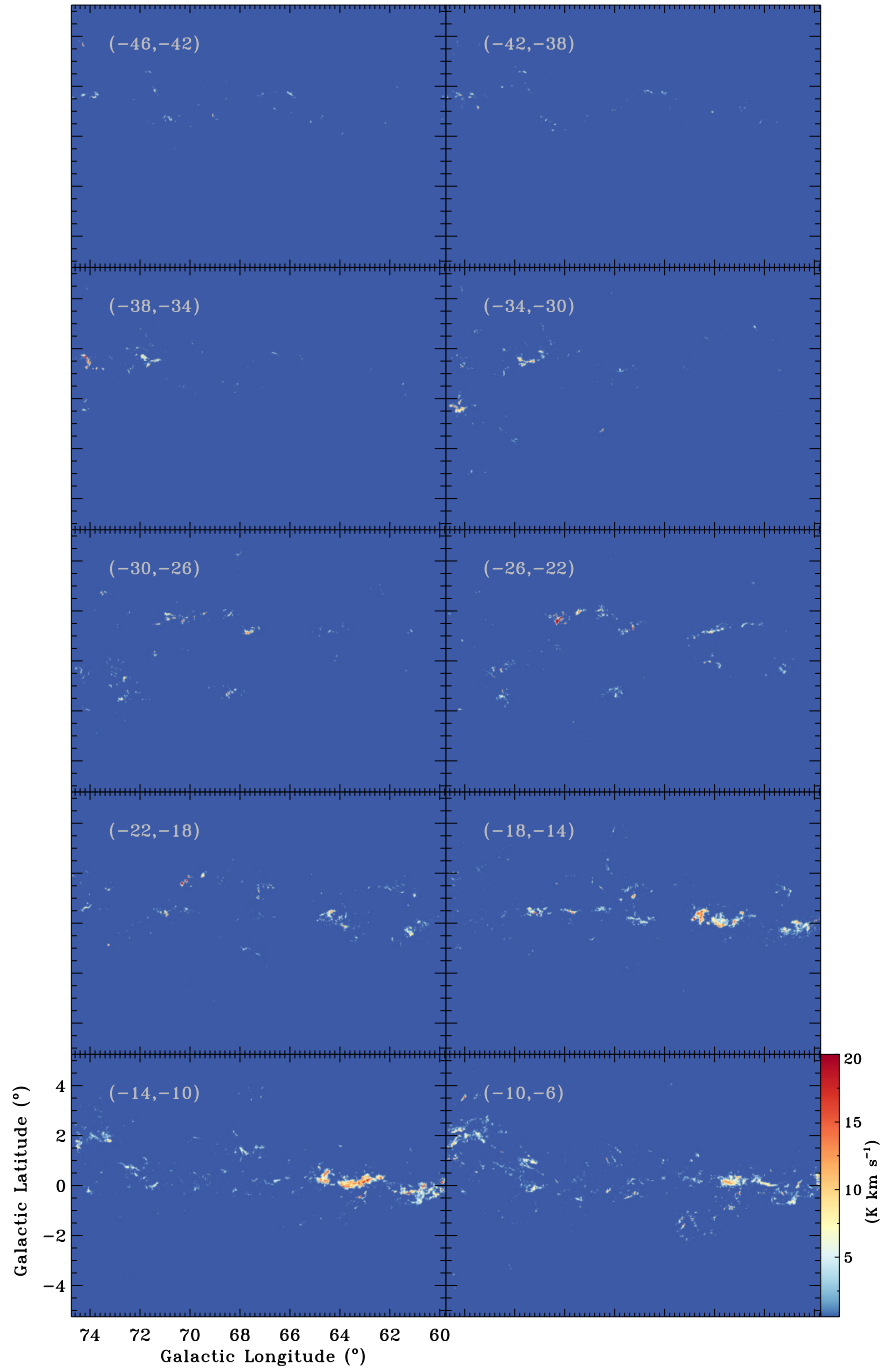


**Figure 15.** Velocity channel maps of  $^{12}\text{CO}$  from  $-45$  to  $-8 \text{ km s}^{-1}$  of the Perseus arm. The velocity range of each channel is shown at the top-left corner of each panel.

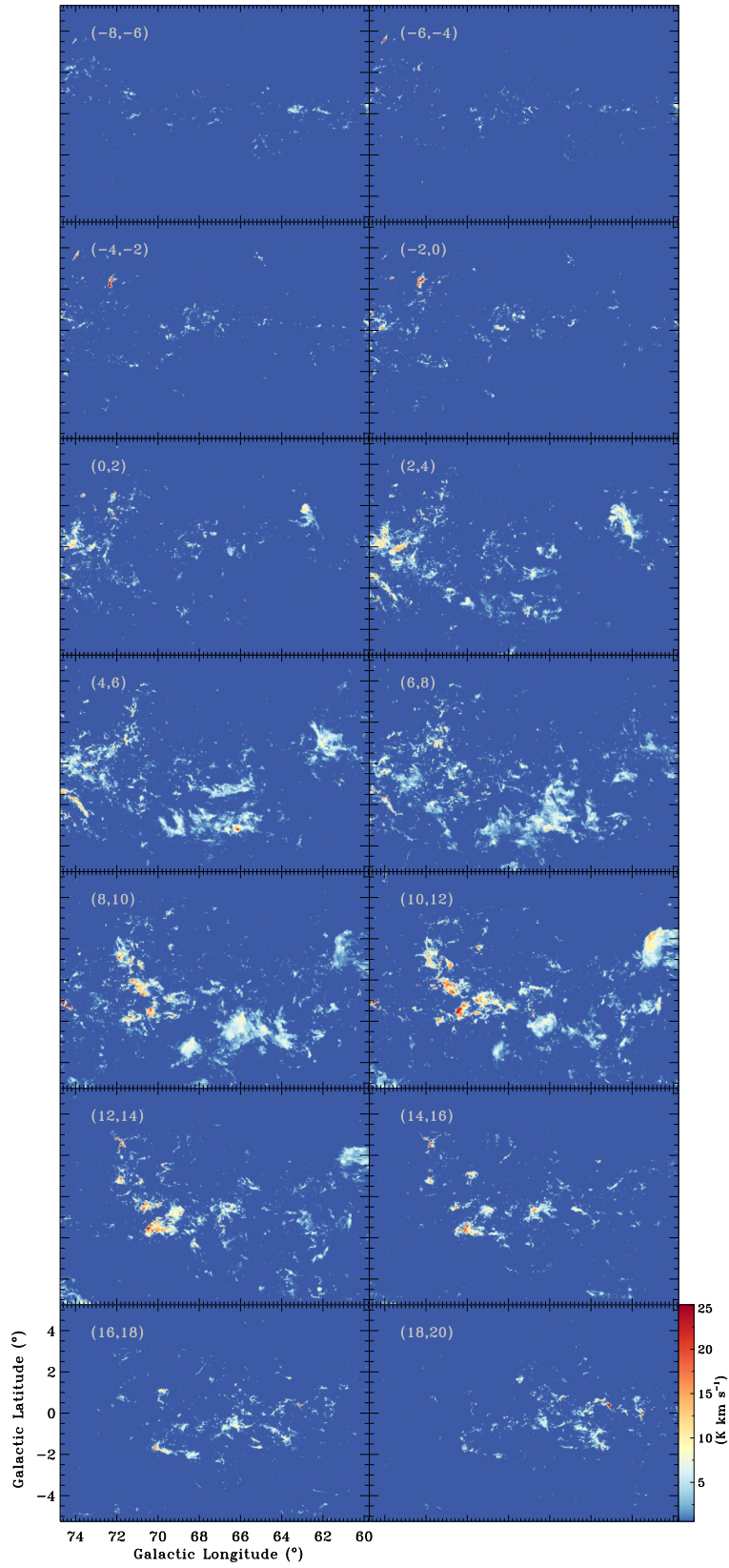


**Figure 16.** Velocity channel maps of  $^{12}\text{CO}$  from  $-8$  to  $20 \text{ km s}^{-1}$  of the Local arm. The velocity range of each channel is shown at the top-left corner of each panel.

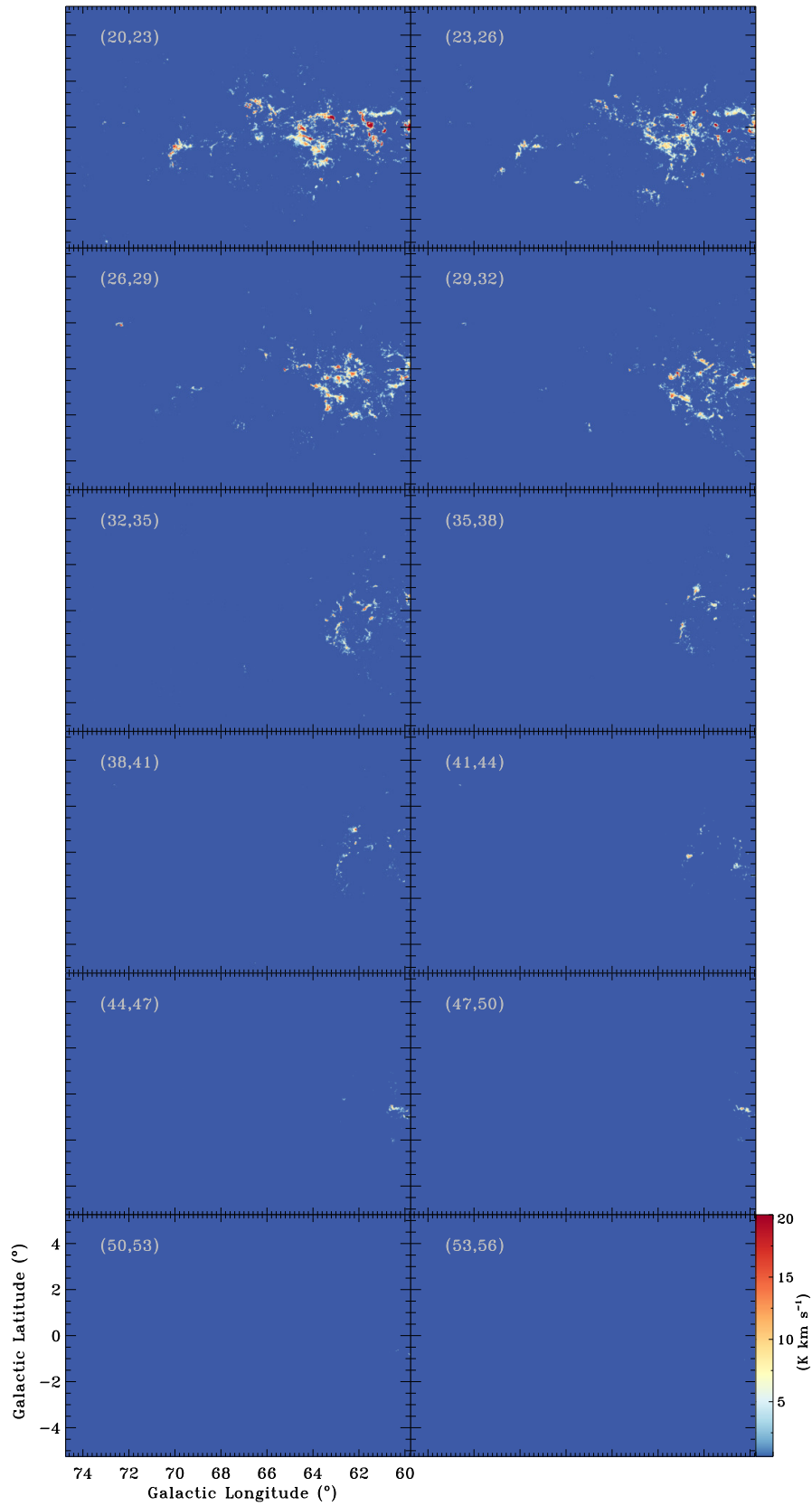


**Figure 17.** Velocity channel maps of  $^{12}\text{CO}$  from 20 to 55  $\text{km s}^{-1}$  of the Local Spur. The velocity range of each channel is shown at the top-left corner of each panel.

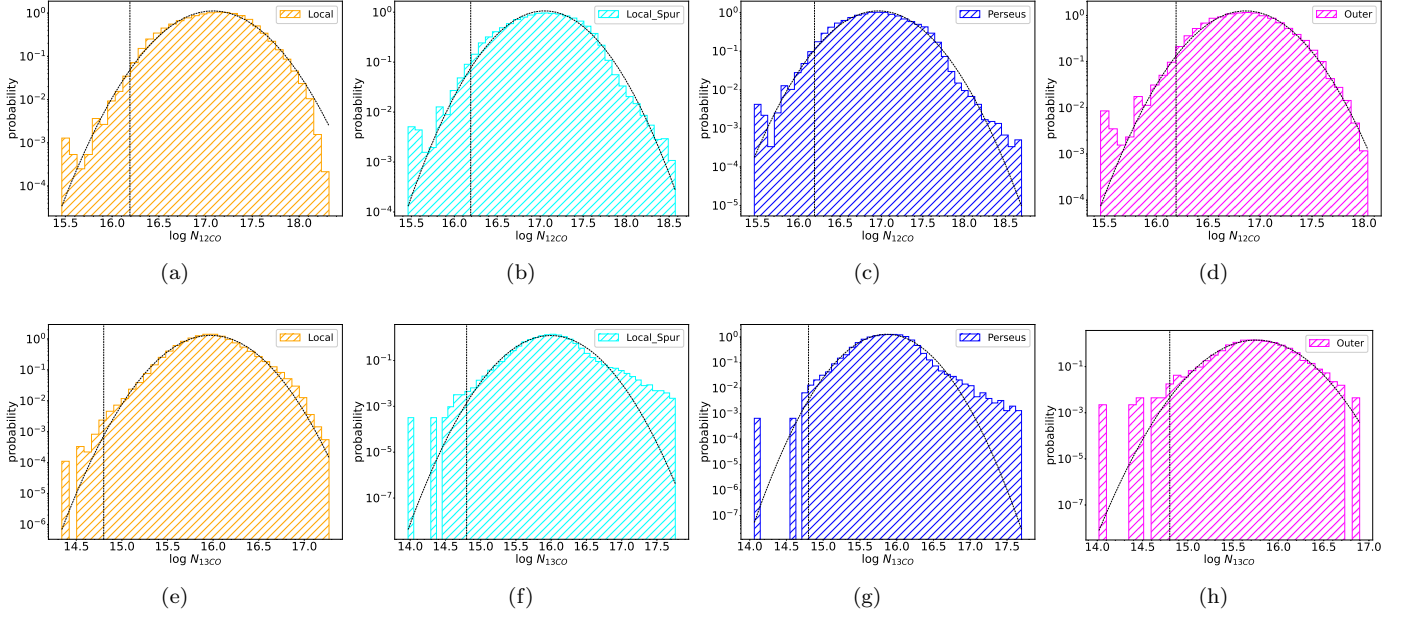


**Figure 18.** Distributions of  $^{12}\text{CO}$  (top row) and  $^{13}\text{CO}$  (bottom row) column densities for each spiral arm individually in the log-log space, overlaid with log-normal functions fit to the data. The vertical dashed line represents the reference detection limit of the molecular gas column density.

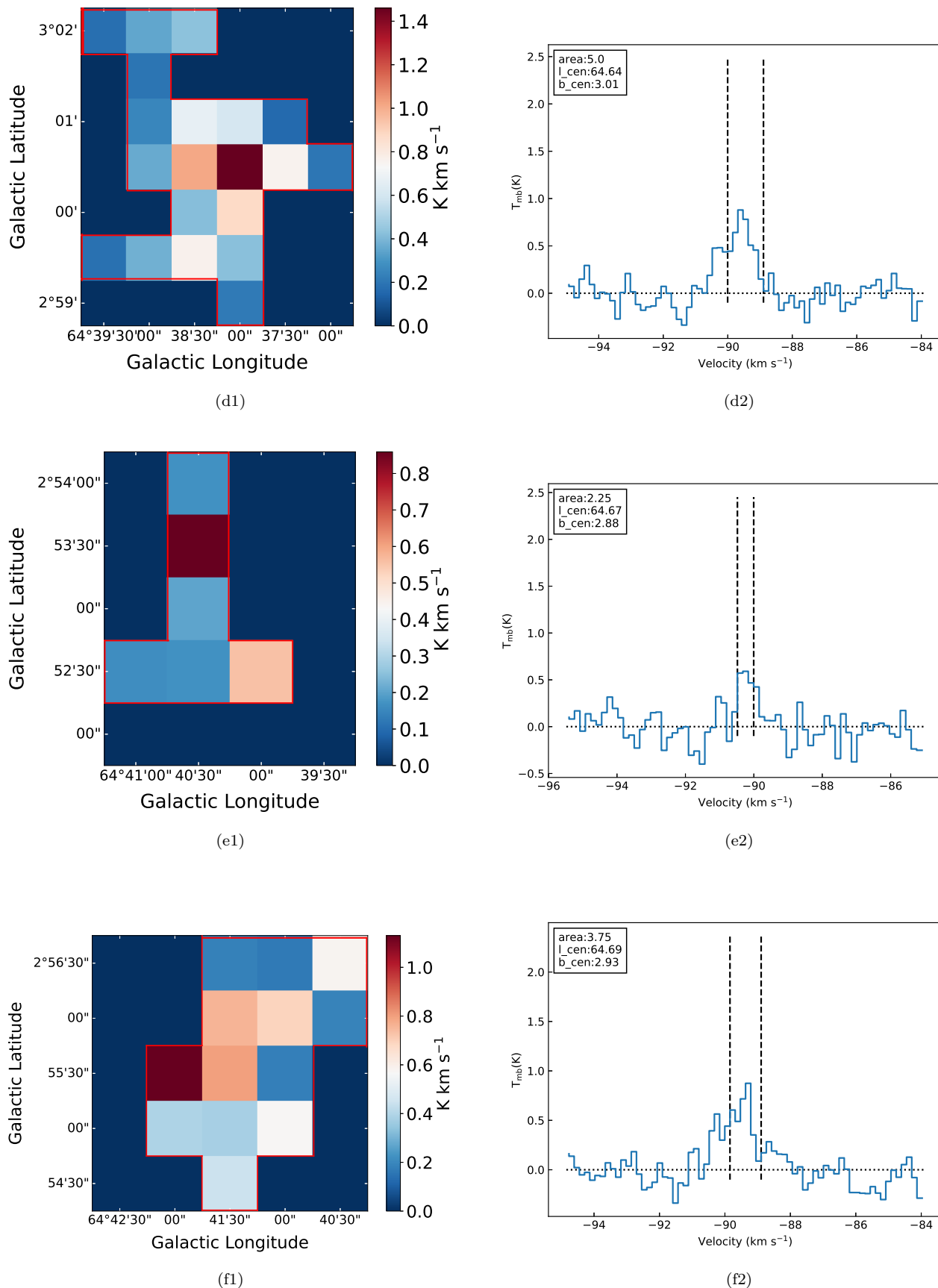
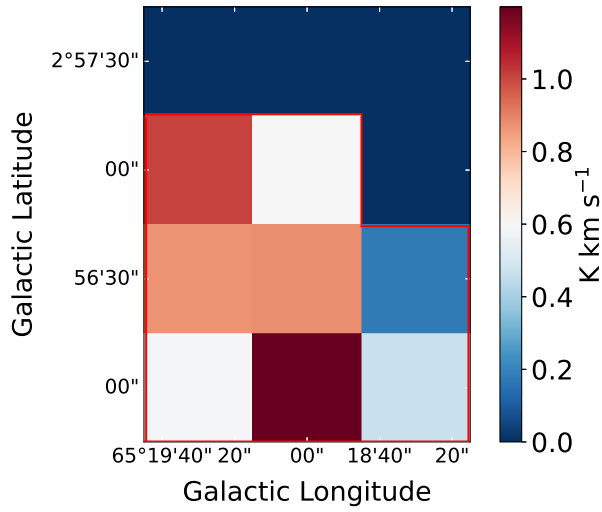
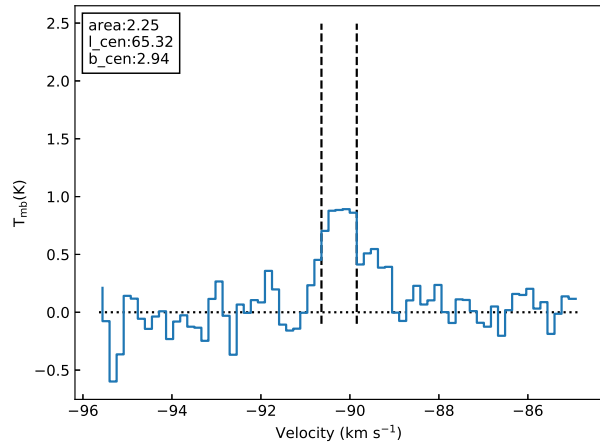


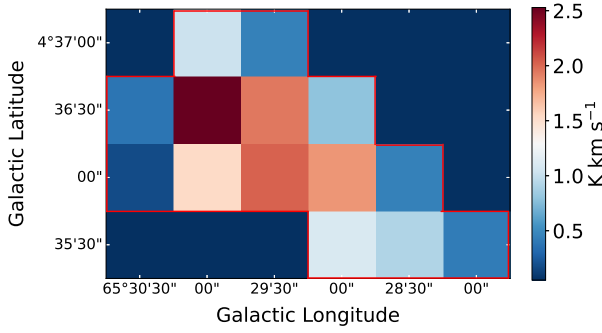
**Figure 19.** Same as Figure 9, but for the other 12 extremely distant molecular clouds in the OSC arm.



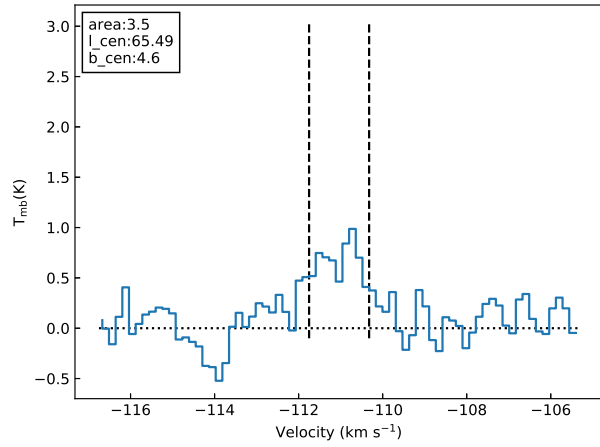
(g1)



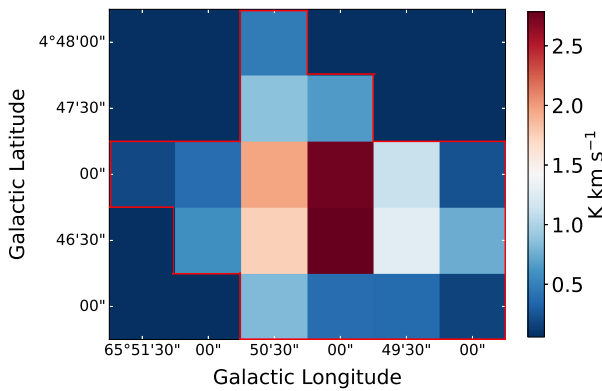
(g2)



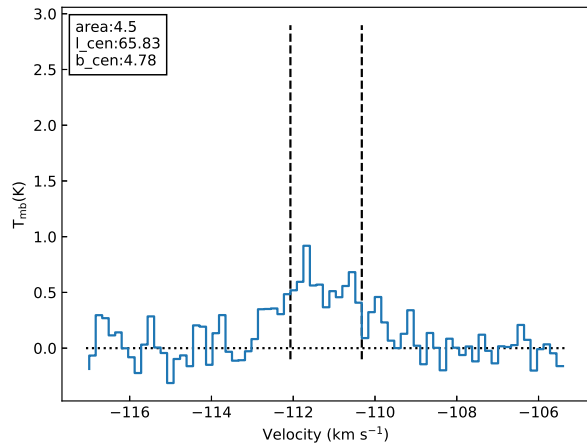
(h1)



(h2)

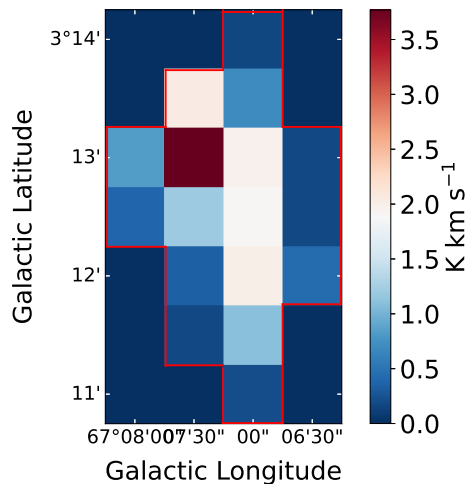


(i1)

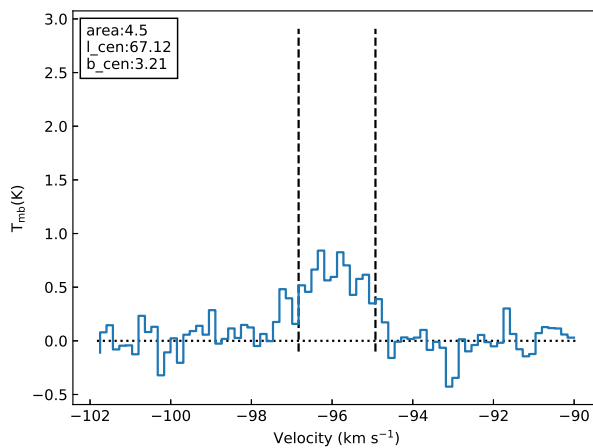


(i2)

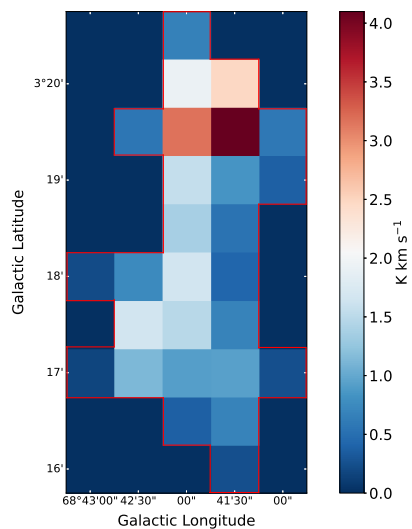
Figure 19. Continued



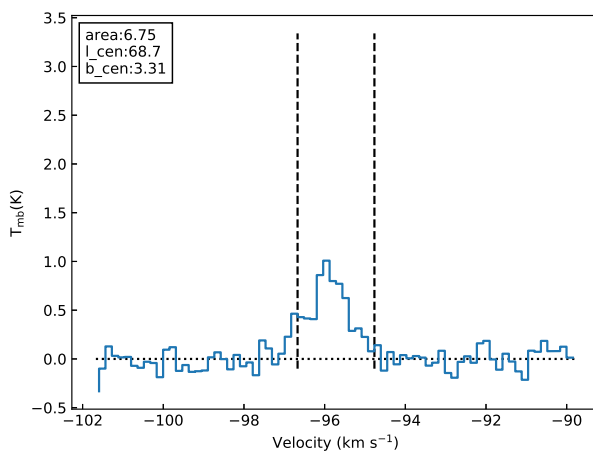
(j1)



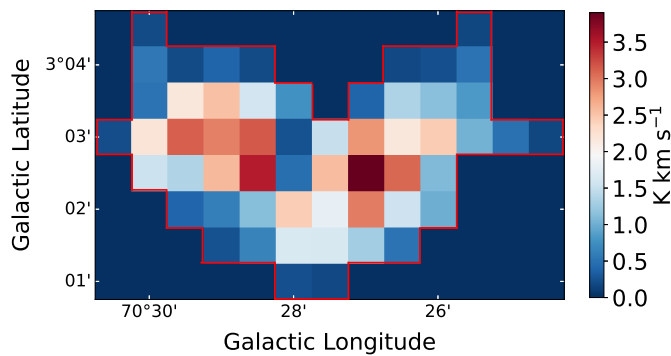
(j2)



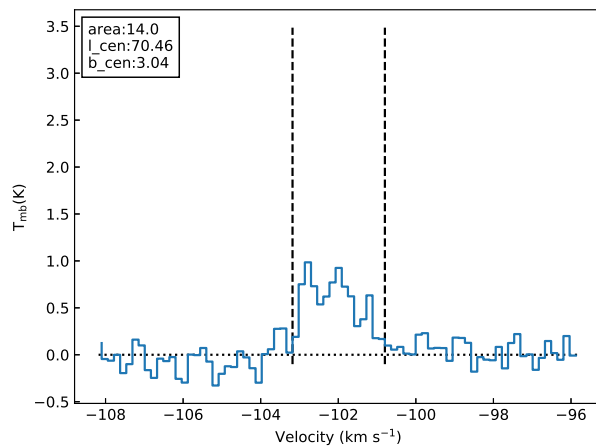
(k1)



(k2)



(l1)



(l2)

Figure 19. Continued



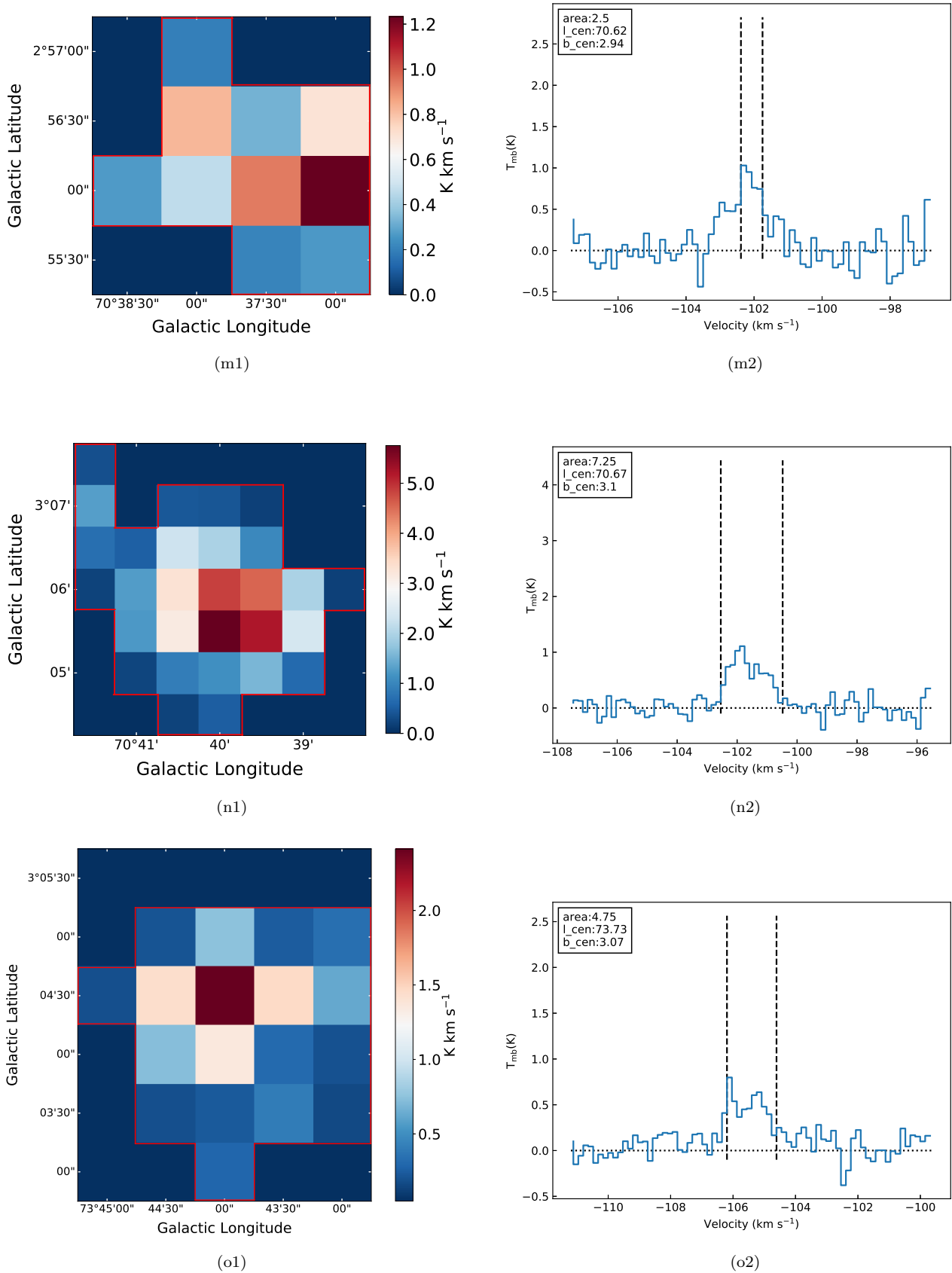


Figure 19. Continued